

# Design principles of crystalline silicon/CsGeI<sub>3</sub> perovskite tandem solar cells using a combination of density functional theory and SCAPS-1D frameworks

Babban Kumar Ravidas<sup>a</sup>, Abhijit Das<sup>b</sup>, Suneet Kumar Agnihotri<sup>c</sup>, Rahul Pandey<sup>d</sup>, Jaya Madan<sup>d</sup>, M. Khalid Hossain<sup>e</sup>, Mukesh Kumar Roy<sup>a</sup>, D.P. Samajdar<sup>b,\*</sup>

<sup>a</sup> Department of Natural Science, PDPM Indian Institute of Information Technology, Design and Manufacturing, Jabalpur, 482005, India

<sup>b</sup> Department of Electronics and Communication Engineering, PDPM Indian Institute of Information Technology, Design and Manufacturing, Jabalpur, 482005, India

<sup>c</sup> Dept. of ECE, BMS Institute of Technology & Management, Bengaluru, Karnataka, 560064, India

<sup>d</sup> VLSI Centre of Excellence, Chitkara University Institute of Engineering and Technology, Chitkara University, Punjab, India

<sup>e</sup> Institute of Electronics, Atomic Energy Research Establishment, Bangladesh Atomic Energy Commission, Dhaka, 1349, Bangladesh

## ARTICLE INFO

### Keywords:

Tandem solar cell  
Perovskites  
CsGeI<sub>3</sub>  
c-Si  
DFT  
SCAPS-1D  
Lead-free perovskite

## ABSTRACT

Perovskite solar cells have become the main source of attraction among photovoltaic researchers since its inception in 2009 due to their steady enhancement in efficiency and cost-effective fabrication methodologies. The integration of the concept of multijunction or tandem technology with Perovskite solar cells is considered to be one of the best substitutes for designing efficient Solar Cells. Recently, the perovskite/silicon tandem architecture possesses tremendous research potential owing to their capability to generate competitive efficiencies. In this research article, we have analysed the optoelectronic properties of CsGeI<sub>3</sub> with the WIEN2K tool for first principle computations through the density functional theory methodology. The bandgap of CsGeI<sub>3</sub> is found out to be 1.6 eV. Calculated bandgap and absorption coefficient spectra are used as input parameters for device simulation using the SCAPS-1D tool. Environment-friendly CsGeI<sub>3</sub> and c-Si are used as top cell and bottom cell absorbers respectively with the two cells connected in series with an ITO interconnecting layer for the proposed tandem solar cell architecture. Under current matching scenario and AM 1.5G spectrum illumination, the standalone top cell shows PCE of 18.31 %,  $V_{oc} \sim 1.20$  V,  $J_{sc} \sim 17.55$  mA/cm<sup>2</sup> and FF  $\sim 86.42$  % for 265 nm thick CsGeI<sub>3</sub> layer, while bottom cell when subjected to the spectrum transmitted by top cell, provided a PCE of 10.15 % with  $V_{oc} \sim 0.703$  V,  $J_{sc} \sim 17.50$  mA/cm<sup>2</sup> and FF  $\sim 82.62$  % with 400  $\mu$ m thick c-Si absorber. Before being implemented in the tandem configuration, simulated J-V characteristics of both top and bottom cells are calibrated to show close agreement with the experimental results. The two-terminal tandem device demonstrates an improved PCE of 28.43 %, FF of 84.90 %,  $J_{sc}$  of 17.55 mA/cm<sup>2</sup>, and  $V_{oc}$  of 1.90 V. The effect of  $R_s$  and  $R_{sh}$  and the interfacial and bulk defect states on the photovoltaic parameters (PCE, FF,  $J_{sc}$ , and  $V_{oc}$ ) is also analysed. Finally, a semi-analytical model is used to validate the J-V characteristics of the tandem architecture obtained with SCAPS-1D simulator using an equivalent circuit model of two series-connected diodes. This study can open new directions for the design of eco-friendly lead-free perovskite/c-Si based tandem devices with superior photovoltaic characteristics.

## 1. Introduction

Solar energy is an abundant and non-polluting source of energy that can reduce toxic carbon emissions to a large extent and meet the fast-growing energy demands as well. Only about 0.02 % of the energy available from the solar radiation incident on the earth needs to be

harvested to suffice our energy requirements [1]. In order to harness the maximum energy, researchers are continuously devising new ways to make solar electricity even cheaper and more effective, thereby reducing the dependency on non-renewable sources of energy [2]. The third generation of solar cells (SCs) comprising of emerging photovoltaic (PV) technologies makes use of novel materials in the form of organic,

\* Corresponding author.

E-mail address: [dipprakash010@gmail.com](mailto:dipprakash010@gmail.com) (D.P. Samajdar).

<https://doi.org/10.1016/j.solmat.2023.112688>

Received 22 March 2023; Received in revised form 29 November 2023; Accepted 26 December 2023

Available online 18 January 2024

0927-0248/© 2024 Elsevier B.V. All rights reserved.

perovskite, and dye-sensitize materials in order to cut down the cost of processing involved in the fabrication of SCs utilizing these materials in the absorber layer. Though a reduction in cost has been achieved with these materials, the main concern is their unstable nature in the presence of heat, moisture, or light, which hinders their large-scale commercialization [3]. Perovskite solar cells (PSCs) have helped to achieve a competitive power conversion efficiency (PCE) of 25.5 % recently, since its inception in 2009 with a meagre PCE of only ~3 % [4,5]. This is made possible with the usage of lead-based perovskite (PVSK) materials as absorbers but the toxicity of lead is a major issue [6]. The maximum PCE that can be achieved with an inorganic semiconductor having a band gap ( $E_g$ ) of ~1.1 eV is 48 % as per the detailed Shockley-Queisser limit considering the spectral losses only. However, in the presence of Blackbody radiation effects and lossy recombination mechanisms, the PCE reduces drastically to ~30 % [7]. Though the crystalline silicon (c-Si) based SCs are still dominating the PV industry, the PCE of such SCs have reached its saturation limit and is hovering around 27 %. This value is close to its maximum theoretical efficiency of 29.4 % in the presence of radiative and Auger recombination losses and hence there is almost no room for improvement of PCE [8]. On the contrary, lead-free halide perovskites have demonstrated much lower PCE of ~14 % till date, which can be improved substantially by adopting novel fabrication techniques or suitable design methodologies [9]. The poisonous lead (Pb) atoms can be replaced with Tin (Sn) and Germanium (Ge) due to the similarity in their optoelectronic properties and electronic structure [10]. In addition to this, Ge and Sn-based PVSK absorbers exhibit better antibonding characteristics near the highest occupied molecular orbital (HOMO) in comparison to lead-based absorbers [11]. As the PCE of non-lead-based PSCs is well below the theoretical limit, these can be combined with c-Si based SCs using a tandem configuration to achieve enhanced PCE. It has been established both theoretically and experimentally that Ge can be an appropriate replacement to Pb in halide perovskites owing to its narrow  $E_g$ , superior optical absorption, enhanced conductivity, and mechanical strength [12,13]. It has been predicted theoretically that the maximum PCE that can be achieved with CsGeI<sub>3</sub> (Cesium Germanium Iodide) is ~28 %, which is much higher than the Sn or Pb-based counterparts [14]. This motivated us to select CsGeI<sub>3</sub> as the top cell absorber material but the major concern is the low efficiency of ~5 % for fabricated CsGeI<sub>3</sub> PSCs [15]. Hence, this manuscript is focused on the methodologies to improve the PCE of CsGeI<sub>3</sub> PSCs implemented in tandem configuration with c-Si SCs.

The first monolithic two-terminal (2-T) Methylammonium lead iodide (MAPbI<sub>3</sub>)/Si tandem solar cell (TSC) was demonstrated in 2015, which exhibited PCE of 13.7 %, open circuit voltage ( $V_{oc}$ ) of 1.58 V, short circuit current density ( $J_{sc}$ ) of 11.5 mA/cm<sup>2</sup> and fill factor (FF) of 75 %. Though this PCE is much lower as compared to the best efficiency obtained with PSCs or c-Si SCs, it was predicted that through proper selection of carrier transport materials, surface passivation techniques and improvement of the quality of PVSK layer, efficiencies surpassing 35 % can be achieved with monolithic TSCs [16]. It has been predicted theoretically that the maximum theoretical efficiency of a 2-T perovskite/Si tandem can be ~35.7 % under ideal conditions of zero parasitic absorption and 100 % Internal Quantum Efficiency [17]. It is evident that majority of the research works on lead-free perovskite/Si TSC is based on theoretical design and optimization and there are limited reports on experimental fabrication [18–21]. Simulation studies show that optimized structures of four and six-terminal CsSn<sub>1-x</sub>Ge<sub>x</sub>I<sub>3</sub>/Si TSCs exhibit PCEs of 26.9 % and 28.2 %, respectively [18]. A 2-T monolithic lead-free TSC comprising of MASnI<sub>3</sub> with  $E_g$  of 1.3 eV and MASnBr<sub>2</sub> with an  $E_g$  of 1.75 eV as top and bottom (T&B) cells respectively exhibited a PCE of 15.66 % [18]. The J-V characteristics of the standalone T&B cells are calibrated with experimental data before carrying out the systematic numerical investigation.

In this study, we thoroughly studied the structural, electronic, and optical properties of top cell absorber layer CsGeI<sub>3</sub> by density functional theory (DFT). The optoelectronic properties such as the  $E_g$  and

absorption coefficient data are imported into SCAPS-1D (Solar Cell Capacitance Simulator) for numerical investigation on CsGeI<sub>3</sub> based PSC. The photovoltaic parameters of the standalone CsGeI<sub>3</sub> and c-Si single-junction cells are calibrated with experimentally measured data before integrating them in a 2-T TSC configuration. The aim of this study is to discuss the potential of the CsGeI<sub>3</sub> PVSK for designing the next-generation, non-toxic lead-free, and stable TSCs using simplified architectures without compromising the PCE. We have optimized the thickness of the PVSK layer to achieve the current matching condition with the bottom c-Si SC for maximum PCE. Further, the effect of series resistances ( $R_s$ ) and shunt resistances ( $R_{sh}$ ), interfacial and bulk defects on the PV parameters are thoroughly investigated. J-V and Quantum Efficiency (QE) characteristics of the standalone and tandem devices are analysed. Lastly, we have validated our simulated results with the computed results of a semi-empirical mathematical model based on two series connected SCs.

## 2. DFT computations for CsGeI<sub>3</sub> perovskite

The suitability of a particular PVSK material for PV applications depends entirely on its optoelectronic properties. Hence, the precise calculation of optoelectronic properties of the absorber material for SCs is necessary before carrying out the device simulations. Perdew–Burke–Ernzerhof (PBE) potential and Generalized Gradient Approximation (GGA) exchange correlation function implemented using WIEN2k code is used for the calculations. We analysed the  $\alpha$ -cubic phase of CsGeI<sub>3</sub> to determine its semiconductor properties with a space group of 221 ( $Pm\bar{3}m$ ). Ge atoms occupies the central position in the unit cell inside the octahedron and Cs atoms reside at the corners [22]. Unit cell atoms in Wyckoff coordinates are Cs ( $x = y = z = 0$ ), Ge ( $x = y = z = 0.5$ ), and I ( $x = y = 0.5, z = 0$ ). Lattice constant parameters ( $a = b = c = 6.04$  Å) and lattice angles ( $\alpha = \beta = \gamma = 90^\circ$ ) used in this systematic study are taken from Ref. [23]. Fig. 1 shows the CsGeI<sub>3</sub> unit cell crystal structure generated by the WIEN2k after optimization. For the self-consistency cycle (SCF), we set  $R_{MT} \times K_{MAX}$  as 7.0, where  $R_{MT}$  denotes the muffin tin radius of the constituent atoms and  $K_{MAX}$  is the maximum cut-off rate of wave vector  $k$ . The cut-off energy of -6.0 Rydberg is used to differentiate the valence and core states. Force, energy, and charge convergence criteria are taken to be 1 m Ry/au, 0.010 Ry, and 0.001e respectively for SCF cycle.  $12 \times 12 \times 12$  k-mesh is chosen for CsGeI<sub>3</sub> for reciprocal space integration with 2000 k-points in the Brillouin zones [24].

## 3. Simulation methodology and device structure

To save the time and resources associated with experimentation procedure, simulation and modelling of the designed semiconductor devices is considered to be one of the best approaches in which the experimentalists can draw some definite conclusions from the theoretical computation before fabricating the real structures [25]. The

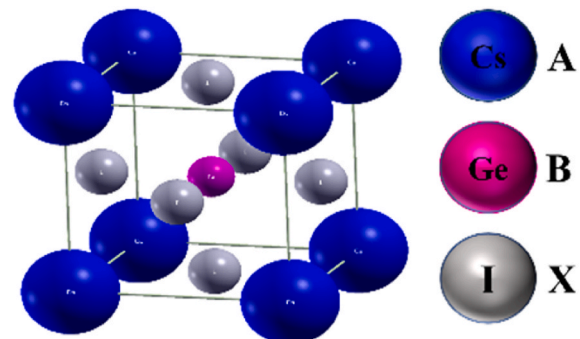


Fig. 1. WIEN2k-generated unit cell of CsGeI<sub>3</sub>.

simulation of the proposed CsGeI<sub>3</sub>/c-Si TSC is carried out using SCAPS-1D software [26]. SCAPS-1D is a versatile and popular tool among researchers as it allows wide variation of the input parameters of materials, thereby making the simulation results promising and close to the experimental results [27]. The basic guiding equations for the simulation of the proposed SCs are the Poisson's and Continuity equations for free charge carriers as shown by (1)-(2) and (3) respectively [28]:

$$\frac{\partial j_n}{\partial t} + G_n(t) - R_n(t) = 0 \quad (1)$$

$$-\frac{\partial j_p}{\partial t} + G_p(t) - R_p(t) = 0 \quad (2)$$

$$\frac{\partial^2 \phi}{\partial t^2} = -\frac{q}{\epsilon_r} [p(t) - n(t) + N_D^+(t) - N_A^-(t) \pm N_i(t)] \quad (3)$$

where  $q$  denotes typically the electronic charge,  $p(t)/n(t)$  represent the corresponding spatial free hole/electron concentration,  $N_i(t)$  represents defect density,  $J_{n/p}$  represents electron/hole current density,  $G_{n/p}$  represents the electron/hole generation rate, and  $R_{n/p}$  represent the recombination rate of the electron/hole.  $N_{D/A}^+(t)$  denotes the ionized donor/acceptor doping density. PCE of the SC is obtained using the PV parameters  $J_{sc}$ ,  $V_{oc}$  and FF and incident power  $P_{in}$  with the help of equations (4-5) [29-31].

$$PCE = \frac{FF \times V_{oc} \times I_{sc}}{P_{in}} \quad (4)$$

$$FF = \frac{P_{max}}{P_{in}} = \frac{I_{max} \times V_{max}}{V_{oc} \times I_{sc}} \quad (5)$$

$P_{max}$  is the output power from the SC.

The sub-cells of tandem device is executed with suitable different material layers and their architecture is described as follows: Si-based bottom cell is basically a p-n heterojunction SC comprising of an intrinsic (i-type) layer and p-type amorphous Silicon (a-Si) layer

deposited over n-type c-Si and i-type and n-type a-Si are grown on the other side of n-Si to form a back surface field (BSF) for reducing recombination effects. The structure is similar to that used in Ref. [32]. The top cell comprises of CsGeI<sub>3</sub> absorber layer sandwiched by Spiro-OMeTAD and TiO<sub>2</sub> as the hole transport layer (HTL) and electron transport layer (ETL) respectively. FTO (fluorine-doped tin oxide) has been used as a transparent conducting layer for front contact and ITO (indium doped tin oxide) is used as intermediate layer between the T&B cells. Ag is used as the back contact for bottom cell. The architecture of the standalone T&B cells and their respective spectrums along with the entire tandem structure is portrayed in Fig. 2.

For the tandem device study, we have assumed that the T&B cells are connected through an ideal interconnecting layer (ICL) comprising of ITO (indium-doped tin oxide) with minimum electrical and optical losses [47,48]. Top cell is irradiated with A.M. 1.5G solar spectrum and the bottom Si-based sub-cell is irradiated with the filtered spectrum transmitted from the top cell [49], which is obtained by using the formula given below in (6) [50]:

$$I(\lambda) = I_0(\lambda) * \exp\left(\sum_{j=1}^4 -\alpha_{mat_j}(\lambda)t_{mat_j}\right) \quad (6)$$

where  $I_0(\lambda) \sim$  incident spectrum,  $I(\lambda) \sim$  filtered spectrum,  $\alpha(\lambda) \sim$  absorption coefficient,  $t \sim$  thickness of the device layers and  $t_{mat_j}$  represents a specific materials layer ( $mat_j = 1, 2, 3$ , and 4 for FTO, Spiro-OMeTAD, CsGeI<sub>3</sub> and TiO<sub>2</sub>). While the absorption coefficient spectra of TiO<sub>2</sub> and Spiro-OMeTAD are taken from SCAPS-1D database, the absorption coefficient of CsGeI<sub>3</sub> is calculated using WIEN2K software for the simulation of the proposed device. The ambient temperature for simulation is kept fixed at 300 K and thermal velocities of  $e^-$  and  $h^+$  are taken as  $10^7$  cm/s for all the layers. The band-to-band recombination rate for the top cell absorber layer is considered as  $10^{-13}$  cm<sup>3</sup>/s and Auger  $e^-$  and  $h^+$  capture coefficient is taken as  $10^{-29}$  cm<sup>6</sup>/s. All other simulation parameters are taken from reported literature after extensive survey and are specified in Table 1. Interface parameters at the heterojunctions and recombination rates of carriers are listed in Table 2. The

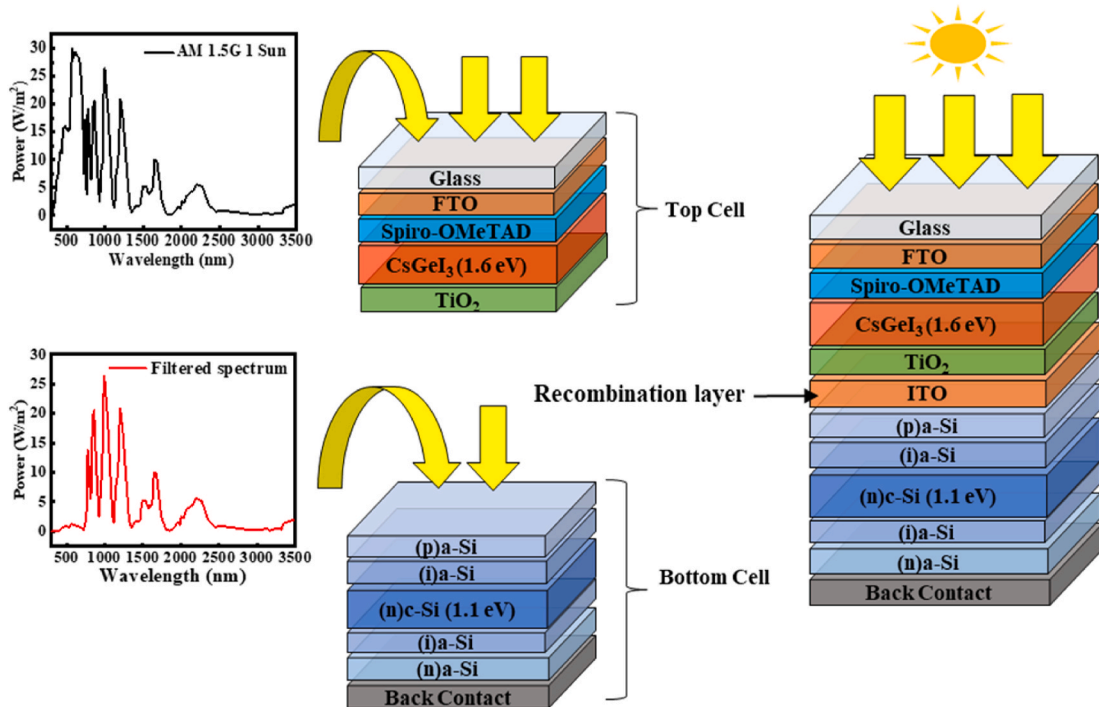


Fig. 2. Schematic structure of CsGeI<sub>3</sub>-on-Si TSC (right). CsGeI<sub>3</sub> top cell is illuminated by AM 1.5G solar spectrum and c-Si based bottom cell is irradiated by the transmitted spectrum (incident solar spectrums are shown in extreme left).

**Table 1**

Input parameters for different layers of both the T&amp;B cells required used for simulation in SCAPS.

Layers Properties	Top Cell				Bottom Cell			
	Spiro-OMeTAD	CsGeI <sub>3</sub>	TiO <sub>2</sub>	ITO	a-Si (p)	a-Si (i)	c-Si (n)	a-Si (n)
Thickness (μm)	0.150	0.1–1	0.030	0.200	0.05	0.05	400	0.05
Band gap $E_g$ (eV)	2.8	1.6	3.2	3.5	1.7	1.7	1.12	1.7
Electron Affinity, $E_A$ (eV)	2.05	3.52	3.9	4.1	3.8	3.8	4.05	3.8
Dielectric Permittivity ( $\epsilon_r$ )	3	18	9	9	11.9	11.9	9	11.9
CB effective DOS $N_C$ (cm <sup>-3</sup> )	$2.2 \times 10^{18}$	$1.0 \times 10^{18}$	$2 \times 10^{18}$	$2.2 \times 10^{19}$	$1 \times 10^{20}$	$1 \times 10^{20}$	$2 \times 10^{18}$	$1 \times 10^{20}$
VB effective DOS $N_V$ (cm <sup>-3</sup> )	$1.8 \times 10^{19}$	$1.0 \times 10^{19}$	$1.8 \times 10^{19}$	$1 \times 10^{19}$	$1 \times 10^{20}$	$1 \times 10^{20}$	$1 \times 10^{19}$	$1 \times 10^{20}$
Electron mobility $\mu_n$ (cm <sup>2</sup> Vs <sup>-1</sup> )	$1 \times 10^{-4}$	20	20	10	20	$1.5 \times 10^3$	$1.5 \times 10^3$	20
Hole mobility $\mu_p$ (cm <sup>2</sup> Vs <sup>-1</sup> )	$2 \times 10^{-4}$	20	10	10	5	$4.5 \times 10^2$	$4.5 \times 10^2$	5
Donor density, $N_D$ (cm <sup>-3</sup> )	0	0	$1 \times 10^{17}$	$1 \times 10^{19}$	0	$1 \times 10^6$	$8 \times 10^{15}$	$1 \times 10^{20}$
Acceptor Density $N_A$ (cm <sup>-3</sup> )	$5 \times 10^{18}$	$1 \times 10^{16}$	0	0	$1 \times 10^{19}$	$1 \times 10^6$	0	0
$N_t$ (cm <sup>-3</sup> )	$1 \times 10^{14}$	$5 \times 10^{14}$	$1 \times 10^{14}$	$1 \times 10^{14}$	$1 \times 10^{16}$	$1 \times 10^{14}$	$1 \times 10^{15}$	$1 \times 10^{16}$
References	[33,34]	[13,35]	[36,37]	[38,39]	[40–43]			

**Table 2**

Parameters for interfacial layers used in simulation [44–46].

Defect location	$N_t$ (cm <sup>-2</sup> )	Defect Energy level $E_t$ (eV)	Defect type	Capture Cross Section of electrons/holes (cm <sup>2</sup> )
CsGeI <sub>3</sub> bulk	$5 \times 10^{14}$	0.6	Neutral	$1 \times 10^{-15}$
c-Si bulk	$1.3 \times 10^{12}$	0.6	Neutral	$1 \times 10^{-15}$
TiO <sub>2</sub> /CsGeI <sub>3</sub> interface	$1 \times 10^{11}$	0.6	Neutral	$1 \times 10^{-19}$
CsGeI <sub>3</sub> /Spiro interface	$1 \times 10^{11}$	0.6	Neutral	$1 \times 10^{-19}$
i-Si/c-n-Si	$1 \times 10^{10}$	0.6	Neutral	$1 \times 10^{-15}$
c-n-Si/i-Si	$1 \times 10^{10}$	0.6	Neutral	$1 \times 10^{-15}$

filtered spectrum is widely used for determining the current matching condition and used to simulate CsGeI<sub>3</sub>/Si tandem device.

## 4. Results and Discussions

### 4.1. DFT analysis of the electronic band structure and optical properties of CsGeI<sub>3</sub>

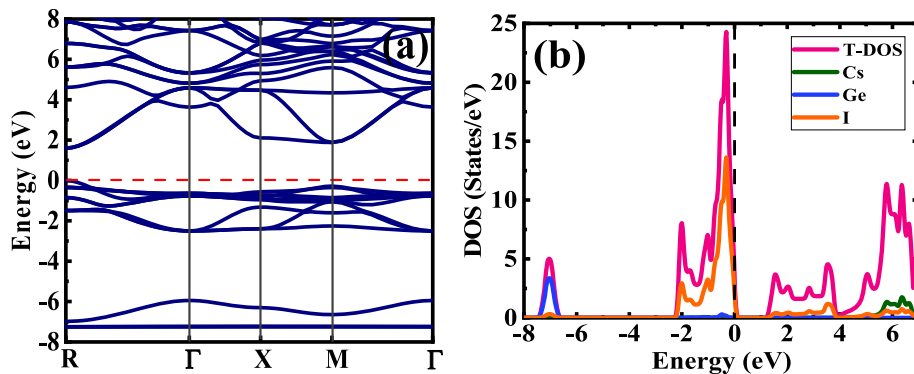
Computational approaches based on DFT are considered as one of the most important tools for predicting the different material properties vividly. Therefore, we have studied the optoelectronic properties of the CsGeI<sub>3</sub> PVSK for its use in photovoltaics. Band structure of CsGeI<sub>3</sub> is depicted in Fig. 3(a). The first principle DFT computations solve the Kohn-Sham equations using an appropriate exchange-correlation (XC) functional and PBE GGA is employed for estimation of solid state structure electron density and compute the band structure of CsGeI<sub>3</sub>

[51]. CsGeI<sub>3</sub> possesses a direct  $E_g$  of 1.60 eV, that is the conduction band minima (CBM) and Valence band maxima (VBM) are positioned at R point and contemplates a k-point route with good symmetry in the Brillouin zone (R - G - X - M - G). Zero energy level indicates the Fermi level. This calculated  $E_g$  is used during the simulation of the device. The band structure can be clearly understood from the interpretation of the DOS. The total DOS (TDOS) and partial DOS (PDOS) of CsGeI<sub>3</sub>, calculated using PBE-GGA co-relation functional is demonstrated in Fig. 3(b). DOS represents the possibility of detecting the presence of electrons within a certain energy range in the crystal. From Fig. 3(b), it is observed that peak of DOS at -2 eV and -7 eV correspond to the VB and CB energy states and TDOS start rising from 1.6 eV, which corresponds to the CB minima and the  $E_g$  of CsGeI<sub>3</sub>. From DOS plot, it is evident that Germanium (Ge) and Iodine (I) atoms contribute majorly to the VB, and the contribution of the Iodine (I) atoms in the VBM near Fermi level is more than Cs and Ge atoms. A small fraction of the Cs and I atoms also contribute to the CB minima.

The study of the optical properties of absorber layer CsGeI<sub>3</sub> is very significant to determine the capability of the material for use in SC applications. Light interaction with matter can help to estimate the optoelectronic characteristics. Absorption of electromagnetic radiation is the process in which matter (usually electrons in atoms) picks up the energy of a photon, and converts the electromagnetic energy of the photons into the internal energy of the absorber [52]. Dielectric function is a crucial parameter to determine the degree of interaction between matter and light. The dielectric function plot of CsGeI<sub>3</sub> is shown in Fig. 4 (a). The complex dielectric function  $\epsilon(\omega)$  describing optical properties, comprises of the real part  $\epsilon_1(\omega)$  and imaginary part  $\epsilon_2(\omega)$  as shown in equation (7) [53].

$$\epsilon(\omega) = \epsilon_1(\omega) + i\epsilon_2(\omega) \quad (7)$$

The real part of the dielectric constant dependent on incoming radiation frequency may correctly describe the dynamical screening

**Fig. 3.** (a) Band structure and (b) DOS of CsGeI<sub>3</sub> computed using DFT.



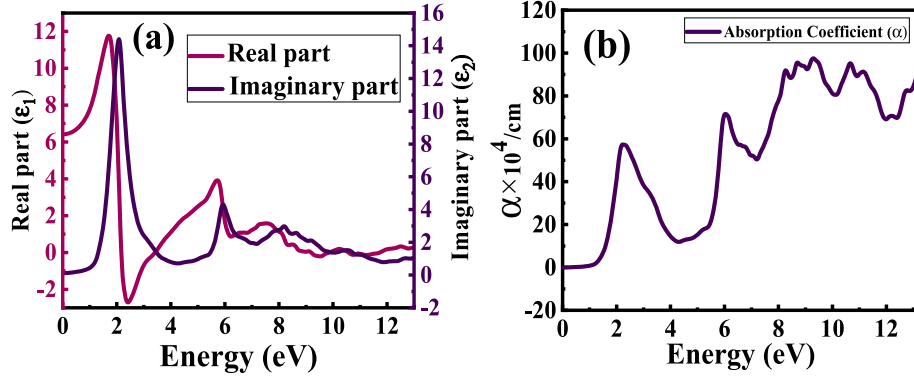


Fig. 4. (a) Represents the complex dielectric function with real and imaginary part, (b) absorption coefficient  $\alpha(\omega)$  of the CsGeI<sub>3</sub>.

effects in materials caused by charge excitations from the matter interacting with radiation. This also depicts the energy storage, photon polarization and dispersion capability of the investigated material. Eq (8) defines the real part  $\epsilon_1(\omega)$  as given below [28]:

$$\epsilon_1(\omega) = 1 + \frac{2}{\pi} p \int_0^{\infty} \frac{\omega' \epsilon_2(\omega') d\omega'}{\omega'^2 - \omega^2} \quad (8)$$

where  $p$  represents the integral's primary value.

The imaginary part  $\epsilon_2(\omega)$  represents the DOS and momentum matrix  $P$ -dependent transitions from occupied to empty states through static  $k$ -vectors across the Brillouin zone.  $\epsilon_2(\omega)$  is defined by eq (9) [51].

$$\epsilon_2(\omega) = \frac{4e^2\pi^2}{m^2\omega^2} \sum_{(i,j)} \int_0^k |M|^2 f_i(1-f_j) \times \delta^2(E_{ij} - E_{ij} - \omega) d^3k \quad (9)$$

where  $M$  is the dipole matrix,  $E$  is the polarization presence of electric field,  $f_i$  is the  $i_{th}$  state of the Fermi level,  $E_i$  represents  $i_{th}$  energy states of electrons, and  $k$  is the crystal wave vector.

The extinction coefficient  $k(\omega)$  and absorption coefficient  $\alpha(\omega)$  from the dielectric constant are computed using the following equations. (10) and (11) [28].

$$k(\omega) = \frac{1}{\sqrt{2}} \sqrt{\epsilon_1(\omega) - \sqrt{\epsilon_1^2(\omega) + \epsilon_2^2(\omega)}} \quad (10)$$

$$\alpha(\omega) = \frac{4\pi E k(\omega)}{hc} \quad (11)$$

where  $E$  is the total energy of the electrons,  $h$  is Planck's constant, and  $c$  is the speed of light.

Fig. 4(b) gives information about the absorption coefficient, which signifies that the proportion of the power of the light that is being transmitted over a material is reduced as a function of distance traversed [54]. From the figure, the absorption peaks show that visible and UV light energy is absorbed in the electromagnetic spectrum. Spectra of  $\alpha(\omega)$  starts to rise from  $\sim 1.6$  eV and increases to reach maximum value at  $\sim 9.5$  eV. CsGeI<sub>3</sub> shows maximum absorption in the range of 1.6–4 eV of the visible spectra. The calculated absorption coefficient spectrum was used during simulation of the device to analyse the photovoltaic parameters.

#### 4.2. Calibration of simulated data with experimental works for validation

Before proceeding for in-depth analysis of the proposed TSC, we have validated the simulated results with reported experimental CsGeI<sub>3</sub>-based PSC and c-Si-based SCs. Firstly, the top CsGeI<sub>3</sub> cell was calibrated with experimental result which reported a low PCE of 4.49 % with  $J_{sc}$  of 18.11 mA/cm<sup>2</sup>,  $V_{oc}$  of 0.51 V and FF of 53.1 % [15]. The performance of

the calibrated device is much below the expected value, and we need to optimize the structural and material parameters such as thickness,  $N_b$ , interface  $N_b$ , doping density,  $R_{ss}$ , and  $R_{sh}$  resistance of the absorber layer in order to achieve enhanced performance out of it. The bottom cell (c-Si) calibrated with a thickness of 400  $\mu$ m has somewhat higher PCE of 24.49 %, which is very near to the experimental reported device of PCE of 24.5 % [55]. The calibrated parameters are compared with the experimentally obtained PV parameters in Table 3. The J-V characteristics of both the simulated and experimental CsGeI<sub>3</sub> and c-Si-based SCs are demonstrated in Fig. 5 (a) and 5 (b) respectively and it is clear from the plots that there is a close match between the experimental and simulated data. We also studied various reports in which the SCAPS-1D model was fitted to experimental data [56–58] and anticipated the increased PV performance of the PSC by optimizing the device layer after altering calibrated parameters.

#### 4.3. Analysis of the energy band diagram (EBD)

The energy band (EB) alignment between the different materials used as absorber or transport layers in the tandem structure are analysed as band alignment is known to have a direct effect on the PV performance. EB alignment of the different layers utilized in the simulation is illustrated in Fig. 6, which represents the electron affinity, energy of the VBM, CBM and work function of the electrodes.

The energy band diagram of the tandem device is depicted in Fig. 7. The T&B cells are positioned below and above the zero value on the x-axis, respectively. 2-T tandem monolithic SC architecture resembles the connection of two diodes in series. Consequently, the  $V_{oc}$  of the TSC is the sum total of the  $V_{oc}$  of the individual cells when operating independently. This tandem configuration requires the flow of equal current through both the T&B sub-cells, which can be achieved through current matching in ICL. In perovskite-silicon tandem SCs, the interconnecting layer commonly chosen for current matching is indium tin oxide (ITO) because of its high transmittance ( $>80$  %) in visible range, low electrical resistance ( $1.5\text{--}2.0 \times 10^{-4} \Omega\text{cm}$ ), wide bandgap (3.5–4.3 eV), and significant work function (4.8 eV), making it an excellent candidate for ICL. ITO also possesses high electron concentration, which results in increased  $V_{oc}$  and FF [48,59–65]. Therefore, in this study, an ideal current matching layer/interconnecting layer consisting of ITO was utilized to ensure current matching between the top and bottom cells.

Table 3

Comparison chart of the experimental and calibrated performance parameters of the studied SC.

Devices	$J_{sc}$ (mA/cm <sup>2</sup> )	$V_{oc}$ (V)	FF (%)	PCE (%)
Si (Simulation)	40.40	0.741	81.77	24.49
Si (Experimental) [55]	40.1	0.741	82.5	24.5
CsGeI <sub>3</sub> (Simulation)	18.11	0.51	53.10	4.94
CsGeI <sub>3</sub> (Experimental) [15]	18.78	0.51	51.0	4.94

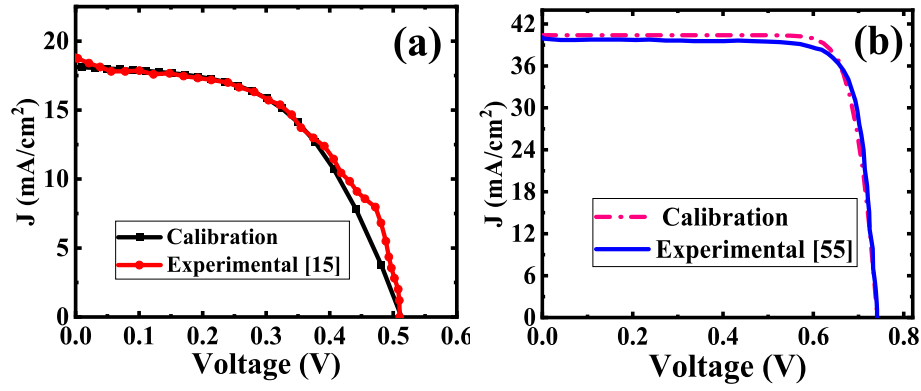


Fig. 5. J-V curve of experimental [15,55] and calibrated device (a) CsGeI<sub>3</sub>-based SC and (b) c-Si-based SC.

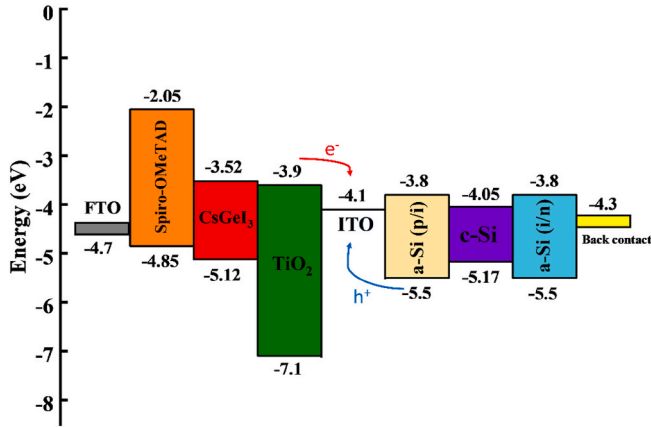


Fig. 6. Schematic band alignment of different layers which represents the electron affinity and VBM of the layer utilized in the simulation of the cell.

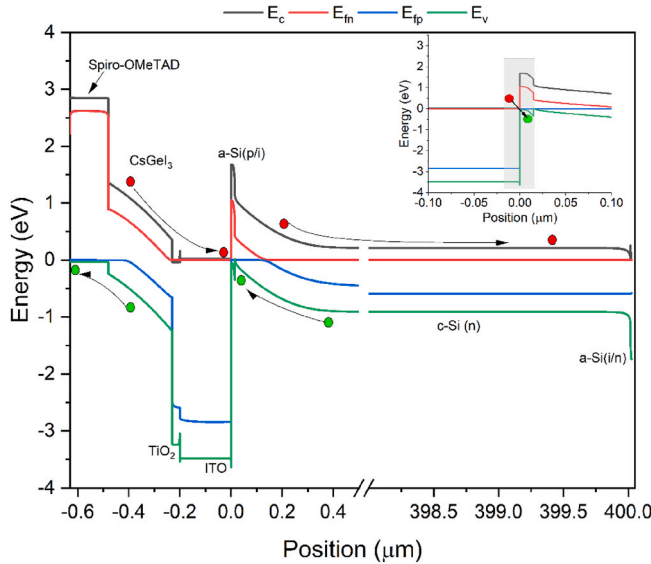


Fig. 7. The generated EBD of the T&B cell in tandem configuration representing the carrier transport mechanism in the device.

Positioned at zero on the x-axis, ITO functions as a current matching interface layer connecting the T&B sub-cells. The EBD of the materials in T&B cells are acquired separately and then combined to generate the complete EBD of the tandem configuration, as illustrated in Fig. 7, where  $E_c$  and  $E_v$  imply the CB and VB, respectively, and  $F_n$  and  $F_p$  are the

respective quasi-Fermi levels. As discussed earlier, the T&B cells are connected with ITO as ICL, and we assume that the ICL is ideal with minimum electrical and optical losses without taking into account the recombination loss processes due to the restrictions imposed by SCAPS-1D software on the usage of ICL [47,49,66,67].

The relative locations of the bands as specified in EBD are crucial for ensuring charge separation across the interface. During light irradiation on the absorber layer of the SC, electron-hole pairs are generated, and the carriers pass through the respective ETL and HTL and are then collected at the contacts. EBD of the T&B cell is achieved in non-equilibrium under AM1.5 illumination at 300 K. The observed split of the Fermi level upon exposure to light confirms the production of electron-hole pairs within the absorber layer [43]. The statement suggests that the photons that were absorbed have supplied sufficient energy to stimulate electrons and generate charge carriers that can be transferred between the sub-cells of the tandem device. The conduction band offset (CBO) between interfaces TiO<sub>2</sub>/CsGeI<sub>3</sub> is small, and due to this reason, photo-generated electrons flow smoothly from the absorber layer to ITO through TiO<sub>2</sub>. The valence band offset (VBO) at the interface between TiO<sub>2</sub> and CsGeI<sub>3</sub> is very high, which blocks the flow of holes to ITO through TiO<sub>2</sub>. On the other hand, the CBO between Spiro-OMeTAD and the CsGeI<sub>3</sub> layer is higher and acts as a barrier, which blocks the electron flow from the absorber CsGeI<sub>3</sub> layer to contact [68]. As the VB energy level ( $E_v$ ) of HTL as Spiro-OMeTAD is greater than the absorber layer, the holes are easily extracted by HTL and are transported to the respective electrode. Additionally, the presence of the ETL/absorber and absorber/HTL interfaces creates a strong enough electric field to split and collect the corresponding charge carriers while restricting the movement of the opposite type of charge carrier [69].

For the bottom cell, c-Si is the absorber layer of the SC, where the electron-hole pairs are generated upon irradiation by light. The electric field generated at intrinsic a-Si/c-Si interface facilitates the separation of the electron-hole pairs. The field exerts a force on the negatively charged electrons, causing them to move towards the n-a-Si layer and are subsequently collected by the metallic back contact situated on the lower surface of the bottom cell [70]. In a similar way, the positively charged holes are pushed towards the p-a-Si layer by the same electric field [42, 71]. Through TSC operation, the holes generated in the c-Si of the bottom cell will be transported through the p-a-Si layer towards the ITO layer. Simultaneously, the electrons generated from the top cell will propagate through the TiO<sub>2</sub> layer to reach the ITO layer. The recombination process at ITO takes place via the band-to-band recombination of electrons and holes, which facilitates the current flow across the tandem device [49].

#### 4.4. Influence of the series resistance ( $R_s$ ) and shunt resistance ( $R_{sh}$ )

In this section, we investigated the impact of the  $R_s$  and  $R_{sh}$  on performance of SC. While  $R_s$  is varied from 1  $\Omega \text{ cm}^2$  to 8  $\Omega \text{ cm}^2$ ,  $R_{sh}$  is varied

from  $10 \Omega\text{-cm}^2$  to  $10^6 \Omega\text{-cm}^2$  to understand the effect of simultaneous variation of both these parameters on the PV performance of the proposed TSC. Fig. 8 (a)–(d) depicts the effect of the variation of  $R_s$  and  $R_{sh}$  on  $J_{sc}$ ,  $V_{oc}$ , PCE and FF. From Fig. 7 (a), it is observed that  $J_{sc}$  declines steadily with the increase in  $R_s$  and becomes almost constant for  $R_{sh}$  beyond  $100 \Omega\text{-cm}^2$ . From Fig. 8 (b), we see that  $V_{oc}$  is independent of the alteration is  $R_s$  but increases with increase in  $R_{sh}$  up to  $100 \Omega\text{-cm}^2$  and beyond that  $V_{oc}$  attains constant value similar to that of the trend followed by  $J_{sc}$ . It is evident from Fig. 8 (c)–(d), PCE and FF decreases from 23.3 % down to 0.7 % and from 86.4 % to 25.0 % on increasing  $R_{sh}$  from  $10 \Omega\text{-cm}^2$  to  $10^6 \Omega\text{-cm}^2$  for a particular value of  $R_s$ . It is observed that PCE and FF increases for  $R_{sh}$  up to  $10^3 \Omega\text{-cm}^2$  but beyond that, both PCE and FF becomes almost constant. The intrinsic  $R_{sh}$  develops due to the recombination in defect levels, and increasing  $R_{sh}$  is equivalent to neutralising the defects states [72].  $R_s$  occurs mostly due to the T&B metal contact layer.  $R_s$  also depends on electrical dissipation in the absorber layers [73]. Ideally,  $R_s$  should be zero and  $R_{sh}$  should be infinite, but to achieve this is difficult, and so to achieve the best performance, we have chosen  $R_s$  as  $1 \Omega\text{-cm}^2$  and  $R_{sh}$  to be equal to  $5 \times 10^4 \Omega\text{-cm}^2$ .

#### 4.5. Effect of thickness variation of CsGeI<sub>3</sub> layer on SC performance parameters

The significance of the change in the thickness of the top cell absorber layer is analysed to extract the best performance out of the TSC. Fig. 9 (a–b) shows the variation of the PV parameters of the standalone top PSC with changing CsGeI<sub>3</sub> layer thickness from 100 nm to 1200 nm. Fig. 9 (a) depicts that the  $J_{sc}$  of the cell increases significantly on increasing absorber layer thickness and saturates thereafter, whereas  $V_{oc}$  increases slightly from 1.197 V to 1.206 V for a thickness range of

100 nm–400 nm and then decreases with further increase in the CsGeI<sub>3</sub> layer thickness. Increased thickness of the absorber layer of the top cell enhances the photon absorption that further increases the photo-generation current in the device. However, increase in the PVSK layer thickness also increases the bulk recombination that restricts the  $V_{oc}$  of the cell [74]. In Fig. 9 (b), note that the FF of the cell declines linearly with increasing CsGeI<sub>3</sub> layer thickness due to rise in  $R_s$  of the SC, whereas the PCE follows a similar trend as that of  $J_{sc}$  with maximum PCE of  $\sim 23.3$  % in the range of 800–1000 nm thickness of the absorber layer.

#### 4.6. Effect of $E_t$ and $N_t$ of the top cell absorber layer on the PSC performance

In this section, we examined the effect of  $N_t$  in the PVSK layer with the variation in the defect energy level of the CsGeI<sub>3</sub> layer constituting the top cell. In the PSCs, the Shockley-Read-Hall (SRH) recombination mechanism depends largely on  $N_t$ , which ultimately influences the device performance [75]. SRH recombination is described by equation (12) [36]:

$$R_{SRH} = \frac{v_{thm} N_t \sigma_n \sigma_p (np - n_i^2)}{\sigma_p [p - p_{td}] + \sigma_n [n - n_{td}]} \quad (12)$$

where,  $v_{thm}$  is the thermal velocity of electrons,  $N_t$  is the volume defect density,  $\sigma_n / \sigma_p$  are the electron/hole capture cross sections,  $n_i$  denotes intrinsic carrier concentration, and  $p_{td}$  and  $n_{td}$  are hole and electron trap densities respectively. We have varied  $N_t$  of absorber layer from  $10^{14} \text{ cm}^{-3}$  to  $10^{17} \text{ cm}^{-3}$ . Fig. 10 depicts the plot of various PV parameters of the PSC as a function of  $E_t$  for different  $N_t$ .

$E_t$  is considered with respect to the VB of CsGeI<sub>3</sub> and increases from

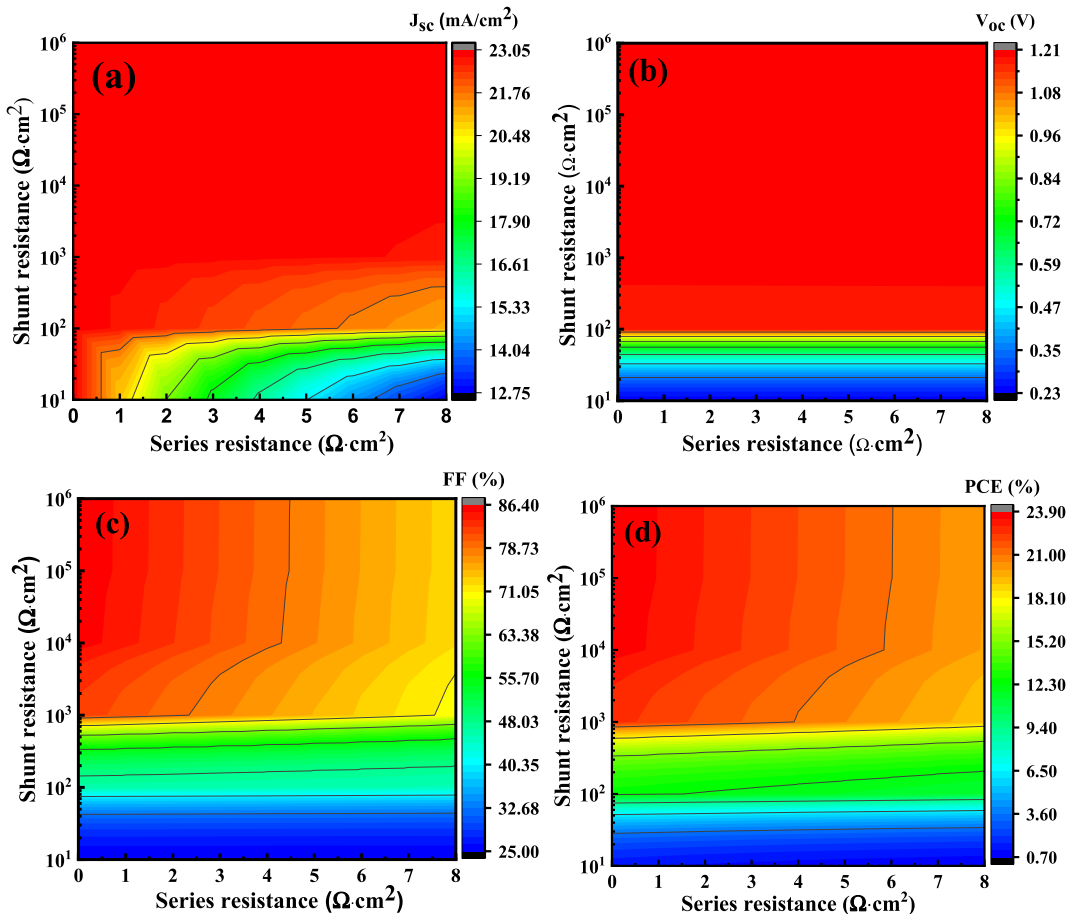


Fig. 8. Contour plots show the effect of the  $R_s$  and  $R_{sh}$  on performance (a)  $J_{sc}$ , (b)  $V_{oc}$ , (c) FF and (d) PCE of the CsGeI<sub>3</sub> top cell.

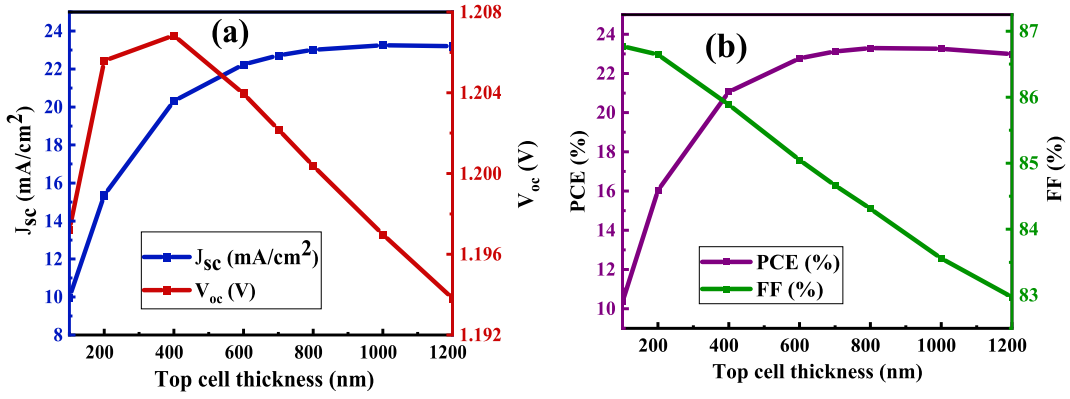


Fig. 9. Effect of absorber layer thickness on (a)  $J_{sc}$  and  $V_{oc}$  and (b) PCE and FF of the top cell.

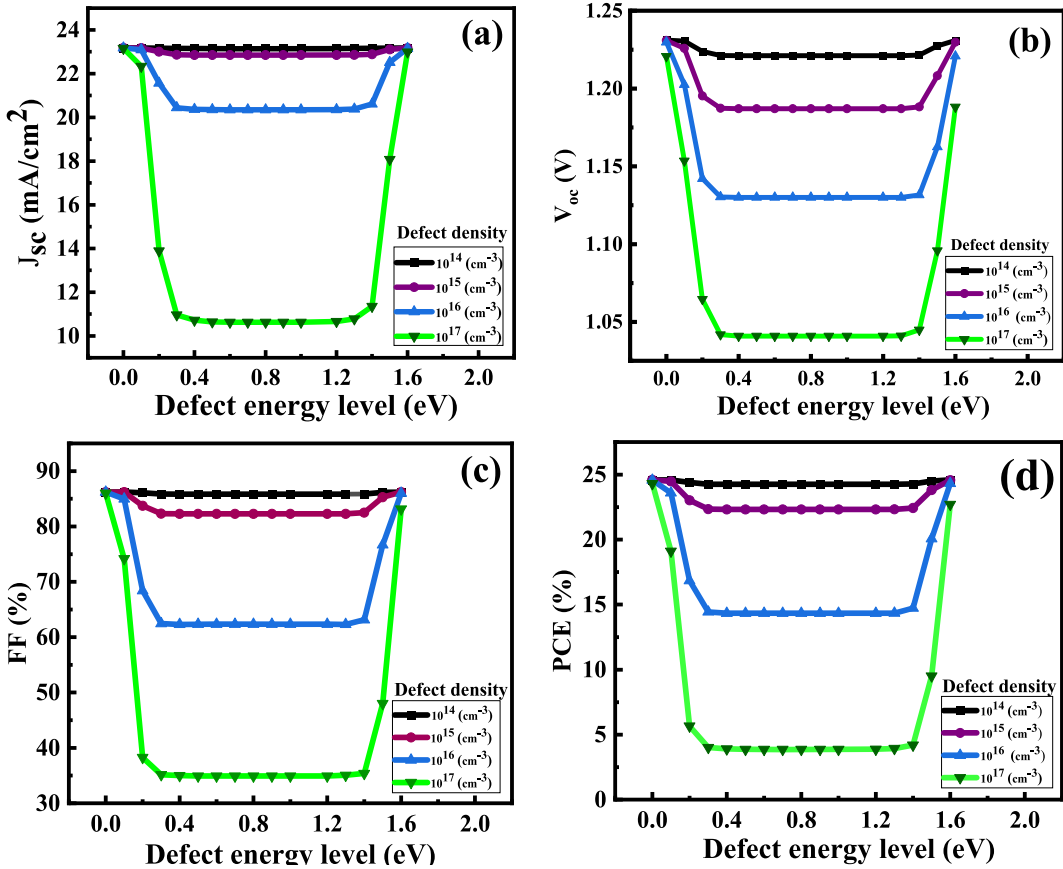


Fig. 10. Effect of variation in defect energy levels on the performance parameters of the top PSC (a)  $J_{sc}$ , (b)  $V_{oc}$ , (c) PCE and (d) FF for four different values of  $N_t$ .

0.2 eV to 1.6 eV. All the four parameters namely  $J_{sc}$ ,  $V_{oc}$ , FF, and PCE of the device declines linearly from 0 to 0.4 eV, and remains constant in the range 0.4–1.4 eV and thereafter increases beyond 1.4 eV. The values of the PV parameters decrease on increasing  $N_t$  which is depicted in Fig. 10 (a-d). As  $N_t$  increases from  $10^{14}$  cm<sup>-3</sup> to  $10^{17}$  cm<sup>-3</sup>,  $J_{sc}$  of the device reduces from 23.17 mA/cm<sup>2</sup> to 10.62 mA/cm<sup>2</sup> and  $V_{oc}$  from 1.23 V to 1.04 V as is evident from Fig. 10(a-b). PCE and FF of the device also reduces from 24.5 % to 3.8 % and 86.1 % to 34.9 % respectively as shown in Fig. 10(c-d). Increasing defect  $N_t$  is equivalent to the increase in the density trap states in the PVSK bulk which results in degradation in performance parameters of the device due to the increase in loss recombination mechanisms and the decrease in the diffusion length of photogenerated charge carriers [76], which deteriorates the  $V_{oc}$  and  $J_{sc}$  of the device.

#### 4.7. Analysis of the interfacial $N_t$ on PSC performance

The interface defects produced by the trap states also play a pivotal role in affecting the device's performance. In this context, the two interfaces namely the CsGeI<sub>3</sub>/HTL and ETL/CsGeI<sub>3</sub> of the top cell comes into consideration. In this section, we have investigated the variation of SC performance parameters on changing the interface  $N_t$  of Spiro-OMeTAD/CsGeI<sub>3</sub> and TiO<sub>2</sub>/CsGeI<sub>3</sub> from  $10^{10}$  cm<sup>-2</sup> to  $10^{18}$  cm<sup>-2</sup>. While Fig. 11 (a-b) show the effect of the variation of the interface  $N_t$  on the PV parameters for TiO<sub>2</sub>/CsGeI<sub>3</sub> interface, Fig. 11 (c-d) show the same for Spiro-OMeTAD/CsGeI<sub>3</sub> interface. From Fig. 10(a), it is clear that  $J_{sc}$  of the top cell decreases from 23.01 mA/cm<sup>2</sup> to 23.004 mA/cm<sup>2</sup> as the TiO<sub>2</sub>/CsGeI<sub>3</sub> interface defect increases from  $10^{15}$  cm<sup>-2</sup> to  $10^{18}$  cm<sup>-2</sup> while  $V_{oc}$  declines from 1.21 V to 0.82 V with increasing interface  $N_t$ .



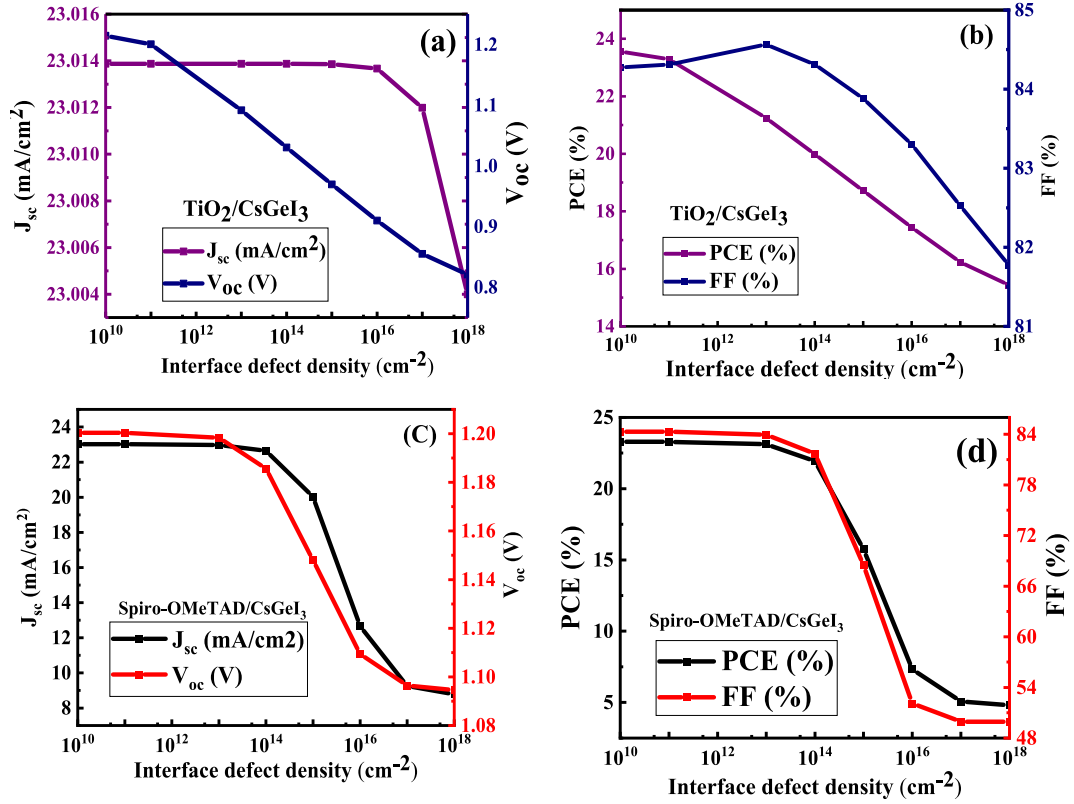


Fig. 11. Effect of the variation of interface  $N_t$  on the PV parameters for (a, b) TiO<sub>2</sub>/CsGeI<sub>3</sub> interface and (c, d) CsGeI<sub>3</sub>/Spiro-OMeTAD interface.

Similarly, from Fig. 11 (b), it is evident that PCE and FF decreases from 23.55 % to 15.44 % and 84.27 %–81.77 % respectively on increasing interface defect from  $10^{10}$   $\text{cm}^{-2}$  to  $10^{18}$   $\text{cm}^{-2}$ . Similar trends in the variation of performance parameters are observed with Spiro-OMeTAD/CsGeI<sub>3</sub> interface. From Fig. 11 (c), it can be observed that  $J_{sc}$  and  $V_{oc}$  of the cell decreases from 23.01 to 23.81 mA/cm<sup>2</sup> and  $V_{oc}$  decreases from 1.2 V to 1.09 V with the increase in interfacial  $N_t$ . Note that PCE and FF also decreases from 23.29 % to 4.80 % and 84.31 %–49.92 % respectively as shown in Fig. 11 (d). From the results, it can be examined that the interface  $N_t$  has stronger effects on  $J_{sc}$  because a major part of carrier generation occurs at the interface. For the Spiro-OMeTAD/CsGeI<sub>3</sub> interface, device performance parameters are not impacted for interface  $N_t$  lower than  $1.0 \times 10^{15}$   $\text{cm}^{-2}$ . Therefore, the tolerable interface  $N_t$  density can be considered up to  $10^{14}$   $\text{cm}^{-2}$ .

#### 4.8. J-V and QE characteristic of optimized top PSC and the bottom c-Si SC

Current density-Voltage (J-V) curve and quantum efficiency (QE) curves of top PSC and bottom cell are depicted in Fig. 12. After optimizing the various structural and material of the top cell PVSK layer, the device structure FTO/Spiro-OMeTAD/CsGeI<sub>3</sub>/TiO<sub>2</sub> exhibits a PCE of 23.29 %, FF of 84.31 %,  $J_{sc}$  of 23.01 mA/cm<sup>2</sup>, and  $V_{oc}$  of 1.20 V. However, the performance metrics of the bottom cell is kept similar to that of the experimentally obtained data with PCE of 24.46 %, FF of 81.82 %,  $J_{sc}$  of 40.40 mA/cm<sup>2</sup> and  $V_{oc}$  of 0.741 V. QE is very important to analyse the performance of the SC and is defined as the ratio of photogenerated carriers collected by the SC to the number of photons incident at a certain wavelength [77]. We varied the wavelength from 300 nm to 900 nm for the top PSC and 300 nm–1200 nm for the bottom c-Si cell. For the top cell, maximum QE of 98.36 % is obtained in the visible range beyond wavelength of 360 nm and drops to zero at

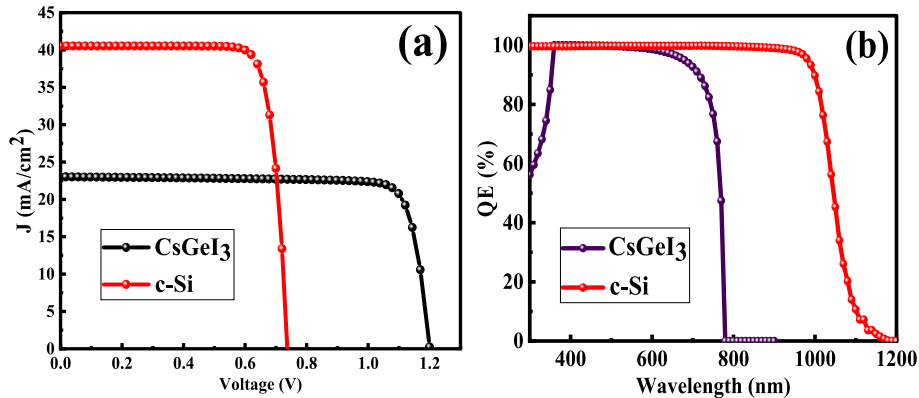


Fig. 12. (a) J-V curve and (b) QE curve of top cell (CsGeI<sub>3</sub>) and (c-Si) cell simulated under full spectrum.

wavelength of 780 nm, which corresponds to the  $E_g$ , equivalent wavelength of CsGeI<sub>3</sub>. For the bottom c-Si cell, a high QE of 100 % in the wavelength range from of 300 nm–1000 nm is obtained, which drops to zero at 1200 nm.

#### 4.9. Effect of the ITO layer bandgap ( $E_g$ ) and electron affinity ( $E_A$ ) on the PSC performance

The interconnecting layer (ICL) in tandem configuration plays a crucial role in estimating the photovoltaic performance of the tandem device. Its significance lies in enhancing the overall performance of both traditional and inverted solar cells by collecting electrons and holes from adjacent sub-cells, facilitating their recombination, and thereby influencing the efficiency of the tandem solar cell. The ICL materials are also expected to exhibit low electrical resistivity and high optical transparency for improved performance. It is important to note that while the ICL's primary role is crucial for device estimation, considerations such as uniformity, mechanical durability, and alignment of the conduction band (CB) and valence band (VB) with the adjacent layers are also essential for optimizing ICL performance [78]. These factors collectively underscore the multifaceted importance of the ICL in tandem solar cell technology.

We have chosen ITO as ICL in the tandem configuration. ITO is a well-known semiconductor with n-type degeneracy and an optical band gap ranging from 3.5 to 4.3 eV. It has a high transparency in the near-infrared and visible regions of the light spectrum [79]. Fig. 13 shows the effect of the bandgap and electron affinity of the ICL layer on the performance parameters of the top cell. We have varied  $E_g$  from 3.4 eV to 4.2 eV of the ICL layer with the corresponding  $E_A$  from 3.4 eV to 4.2 eV. Fig. 13(a) shows the variation of  $J_{sc}$  with  $E_g$  and  $E_A$ .  $J_{sc}$  slightly decreases with increase in bandgap and corresponding increase in

electron affinity. Fig. 13 (b) shows the  $V_{oc}$  variation of PSC and it can be noted that  $V_{oc}$  increases slowly as bandgap increases from 1.145 to 1.207 V, and exhibits a higher value above  $E_g$  of 3.5 eV. Fig. 13(c) and (d) depict that FF increases from 80.60 to 86.42 % and PCE of PSC also increases from 16.19 to 18.31 %. Variations in the  $E_g$  and  $E_A$  of the ICL play a substantial role when  $E_g$  falls below 3.5 eV but become insignificant for  $E_g$  values greater than 3.5 eV. In cases where the ICL possesses a lower bandgap, it tends to absorb a portion of the spectrum prior to allowing the transmission of high-wavelength photons to the bottom cell. And, at lower  $E_g$ , possibility of recombination increases in ICL, which is not suitable for tandem configuration.

#### 4.10. Effect of the defect density ( $N_t$ ) and thickness of ICL on the top cell performances

A solar cell performance is also controlled by  $N_t$  and layer thickness. We have investigated the effect of the  $N_t$  and thickness of ICL on the top cell performance. Fig. 14 displays contour plots of PSC performance metrics as a function of ICL  $N_t$  and thickness.  $N_t$  is varied from  $10^{12} \text{ cm}^{-3}$  to  $10^{18} \text{ cm}^{-3}$  and thickness is varied from 0.05  $\mu\text{m}$  to 0.36  $\mu\text{m}$ . As can be seen from Fig. 14 (a) and (b),  $V_{oc}$  and  $J_{sc}$  show a constant trend across ICL thickness and  $N_t$  and slight variation can be observed in the studied range. Higher  $N_t$  of the ICL can influence the  $V_{oc}$  and  $J_{sc}$  of device slightly, which tends to decrease due to increase in recombination losses. Fig. 14 (c) and (d) present the FF and PCE of the studied TSC. FF shows maximum value at the thickness between 1  $\mu\text{m}$  and 2  $\mu\text{m}$  and effect of  $N_t$  observed is negligible. Maximum PCE is observed at lower  $N_t$  of  $10^{15} \text{ cm}^{-3}$  and higher thickness beyond 2.5  $\mu\text{m}$ . But ICL layer thickness must be lower for transmission of the light from top cell to the bottom cell, and for improved bottom cell performance. Thinner ICL of a tandem solar cell, on the other hand, is a purposeful technique designed

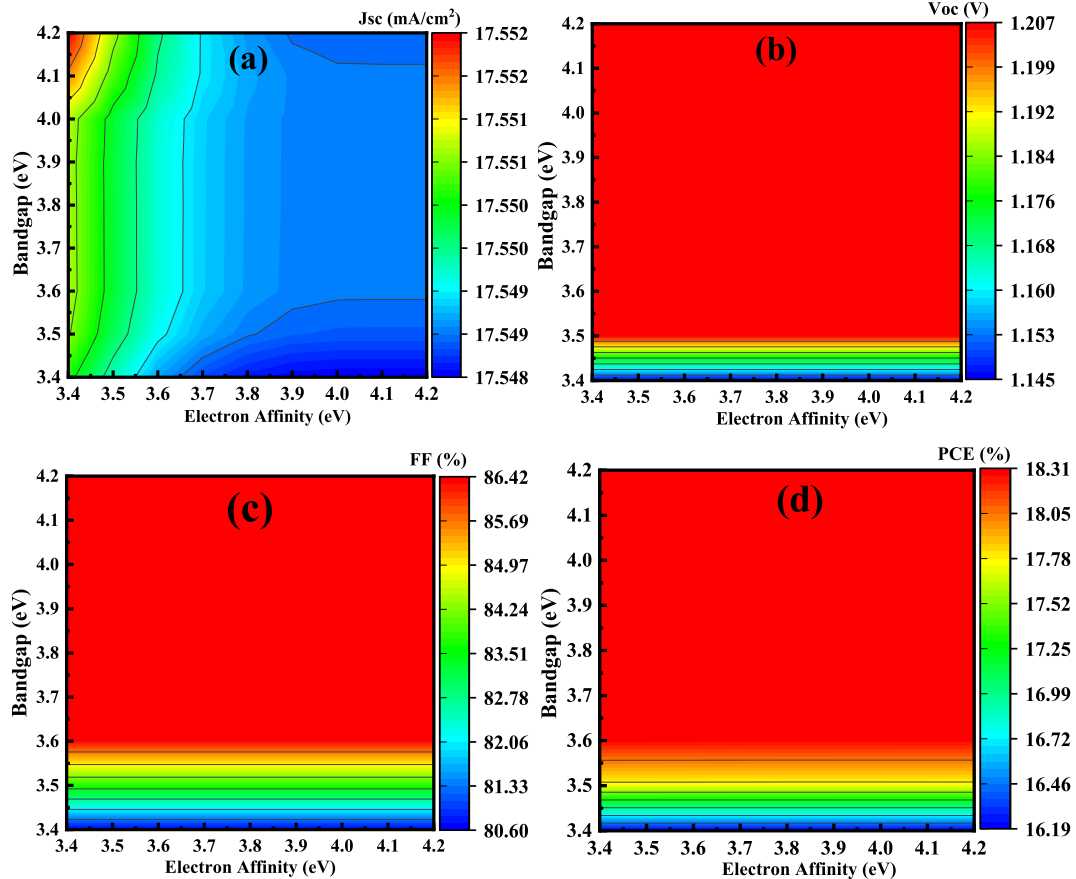


Fig. 13. Contour plots show the effect of the bandgap and electron affinity of the ICL on the top cell performance parameters (a)  $J_{sc}$ , (b)  $V_{oc}$ , (c) FF and (d) PCE.

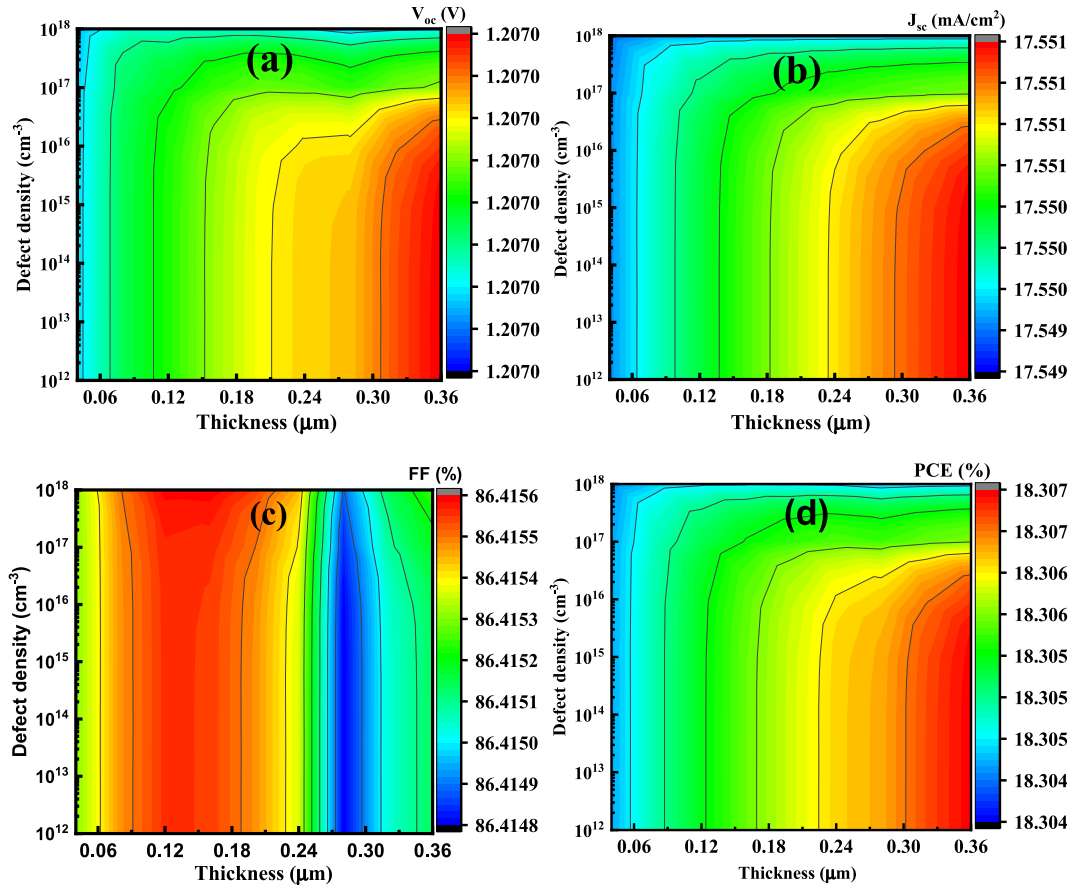


Fig. 14. Contour plots showing the performance of the top cell with the variation in the defect density and thickness of the ICL on (a)  $V_{oc}$ ,  $J_{sc}$ , (b) FF, and PCE of the solar cell.

to maximize light transmission to the bottom cell, thereby boosting its performance and adding to the total efficiency of the tandem structure [78,80].

#### 4.11. Impact of the recombination profile in the ICL on the top cell performance

ICLs play an important role in influencing carrier transport and recombination between the sub-cells in two-terminal monolithic TSCs. As a result, they have a major impact on the overall performance of the TSCs. ICLs play a critical role in addition to preventing charge recombination; they also have the important function of preventing the perovskite solution from infiltrating the bottom cell during the top cell processing [80]. Figs. 15 and 16 show the effect of radiative recombination coefficient ( $B_{rad}$ ) and Auger electron/hole capture coefficient

( $C_n/p$ ) on the PSC performances.

$E_g$  of 3.5 eV and  $E_A$  of 4.1 eV of ICL is fixed for device simulation. We have studied the effect of recombination profile in ICL.  $R_{rad}$  involves the recombining of the free electron from the conduction band to the valence band, and it emits a photon in the bandgap [81]. To examine the effect of  $R_{rad}$ , we change the  $B_{rad}$  factor from  $10^{-11}$  to  $10^{-8}$   $\text{cm}^3/\text{s}$ . A higher value of  $B_{rad}$  factor has a negative impact on the SC performance. All the PV parameters except FF decrease with an increase in the  $B_{rad}$  value as seen in Fig. 15 (a) and (b). For the investigation of the Auger recombination, we have varied  $C_{n/p}$  from  $10^{-25}$  to  $10^{-30}$   $\text{cm}^6/\text{s}$ , as shown in Fig. 16 (a) and (b).  $R_{aug}$  occurs in the semiconductor when the free electron and hole recombine and instantly, the released energy from the recombination is passed to another carrier in VB or CB, which sends the carrier to higher energy levels [15]. As we see, all the PV parameters of the SC except FF show improvement with decreasing value of  $C_n/C_p$ .

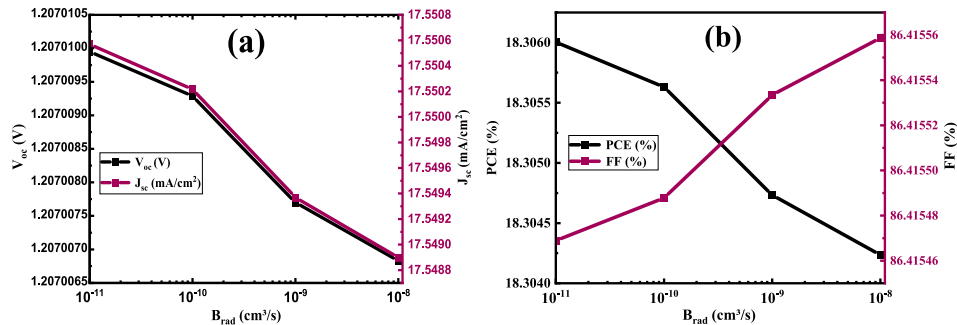
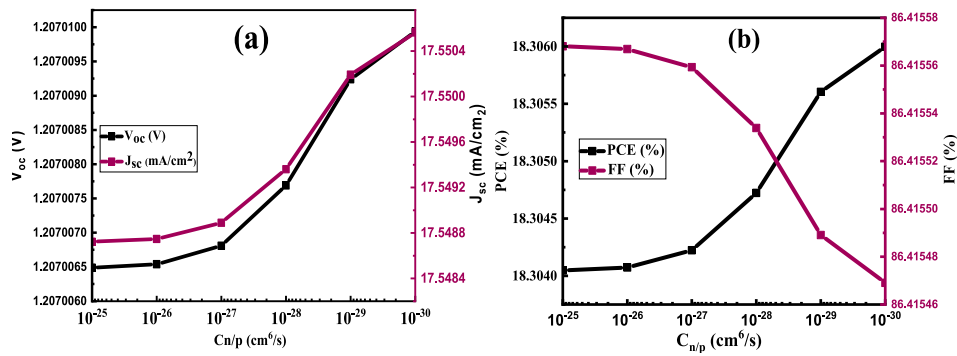


Fig. 15. Performance of a solar cell under radiative recombination ( $R_{rad}$ ); influence of radiative recombination coefficient ( $B_{rad}$ ) on (a)  $V_{oc}$ ,  $J_{sc}$ , (b) FF, and PCE of the solar cell.



**Fig. 16.** Performance of a PSC under Auger recombination ( $R_{aug}$ ); influence of Auger electron/hole coefficient on (a)  $V_{oc}$ ,  $J_{sc}$ , (b) FF, and PCE of the solar cell.

$R_{rad}$  and  $R_{aug}$  depend on the direct and indirect bandgap respectively. So  $R_{rad}$  is more dominant in direct bandgap materials. Variation in the overall performance of the device shows negligible effect with considered parameters of the ICL. For the ideal ICL,  $B_{rad}$  and  $C_n/C_p$  should be lower than 10<sup>-11</sup> cm<sup>3</sup>/s and 10<sup>-26</sup> cm<sup>6</sup>/s.

### 5. Simulation approaches for CsGeI<sub>3</sub>/c-Si tandem device

This section presents the simulation methodology adopted for the numerical analysis of CsGeI<sub>3</sub>/c-Si TSC using SCAPS-1D. The two-terminal TSC can be considered as two series-connected diodes and the current of the T&B cells are made equal through a variation of the absorber layer thickness of both the sub-cells.  $J_{sc}$  value of a TSC is limited by the  $J_{sc}$  value of the sub-cell exhibiting lower  $J_{sc}$  whereas the  $V_{oc}$  is equal to the sum of the  $V_{oc}$  values of the standalone cells [11]. Firstly, the modelled T&B cell are simulated under AM1.5G spectrum with equivalent power density of 1000 W/m<sup>2</sup>. Absorber layer thickness of the top cell is varied from 100 nm to 1000 nm, while the thickness of the ETL and HTL was kept constant. CsGeI<sub>3</sub> based top cell shows good performance after optimization, with PCE of 23.29 %,  $J_{sc}$  of 23.01 mA/cm<sup>2</sup>,  $V_{oc}$  of 1.20 V and FF of 84.31 % for a thickness of 800 nm. While the bottom c-Si cell simulated under A.M 1.5G spectrum at absorber c-Si thickness of 400  $\mu$ m shows PCE of 24.49 % with  $J_{sc}$  of 41.1 mA/cm<sup>2</sup>,  $V_{oc}$  of 0.70 V and FF of 82.5 %, which is almost similar to the experimental data. The power of the transmitted filtered spectrum diminishes as the thickness of the top cell CsGeI<sub>3</sub> layer rises from 50 nm to 500 nm, as can be seen from Fig. 17 (a). These filtered spectra transmitted through various thicknesses of the top cell absorber layer are incident on the bottom c-Si-based SC. Fig. 17 (b) shows the  $J_{sc}$  values of the top PSC illuminated under A.M 1.5G radiation and bottom Si cell simulated under filtered spectrum as a function of CsGeI<sub>3</sub> thickness and gives the current matching condition denoted by the intersection points.

From Fig. 17 (a), it can be observed that initially, the standalone bottom cell has a greater  $J_{sc}$  value than CsGeI<sub>3</sub> top cell. The top cell CsGeI<sub>3</sub> and bottom cell c-Si thicknesses are maintained at a low value of 265 nm and 400  $\mu$ m respectively to achieve the current matching condition of the CsGeI<sub>3</sub>-on-c-Si TSC. At the current matching point, the value of maximum  $J_{sc}$  is 17.55 mA/cm<sup>2</sup>. The top cell current density rises as the top cell CsGeI<sub>3</sub> layer thickness grows, whereas the bottom cell current density drops under the filtered spectrum. Moreover, the top cell under current matching condition exhibits PCE of 18.31 % with  $J_{sc}$  of 17.55 mA/cm<sup>2</sup> and bottom cell under filtered spectrum shows a PCE of 10.15 % with  $J_{sc}$  of 17.50 mA/cm<sup>2</sup>, while the TSC configuration shows improved performance value with PCE of 28.43 %,  $V_{oc}$  of 1.90 V, FF of 84.9 %,  $J_{sc}$  of 17.55 mA/cm<sup>2</sup> respectively. The J-V curves for the TSC (CsGeI<sub>3</sub>-on-c-Si) and the standalone sub cells are depicted in Fig. 18 for a fair comparison of the obtained results. The PV parameters of the top, bottom and tandem devices are listed in Table 4. The CsGeI<sub>3</sub>-on-Si tandem device provides a very feasible nontoxic option for the PSC PV market. Table 5 demonstrates a comparison of some published experimental and numerical simulation performance results of several PVSK-on-Si tandem devices with our work. It can be concluded that our Pb-free device exhibits encouraging results.

#### 5.1. Analysis of the temperature on the tandem device

The temperature is a key factor for the SC performance because SCs usually operate at different environmental temperatures, which may cause fluctuations in the device performance. Moreover, the maintenance of the long-term stability of PSCs under high temperatures is a biggest challenge for the PSC researchers [88]. In this analysis, we have varied the working temperature from 295 K to 340 K to analyse the performance of the TSC. Fig. 19 depicts the J-V curves performance of the TSC for different temperatures. It is evident from the plot that  $V_{oc}$

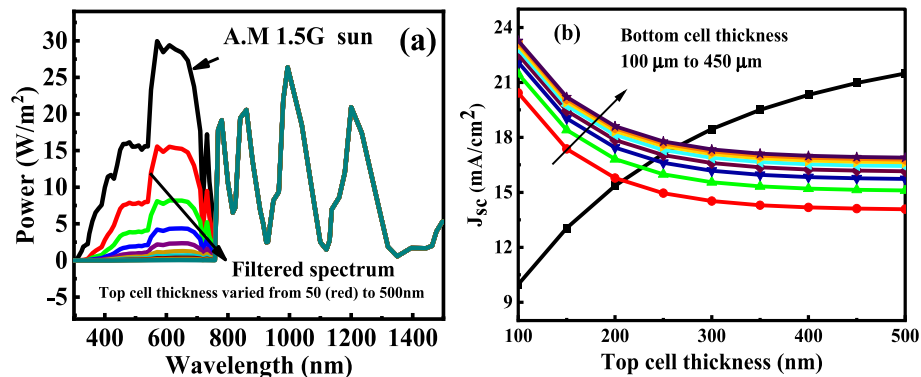


**Fig. 17.** (a) A.M 1.5G solar spectrum incident power and transmitted spectrum through different top cell and (b) Current matching condition obtained through a variation of T&B cell thickness using the filtered spectrum. The intersection points of the bottom (black) and top cell (coloured) give the current matching points and the thicknesses of the bottom and top cell absorber layers for that matched current.

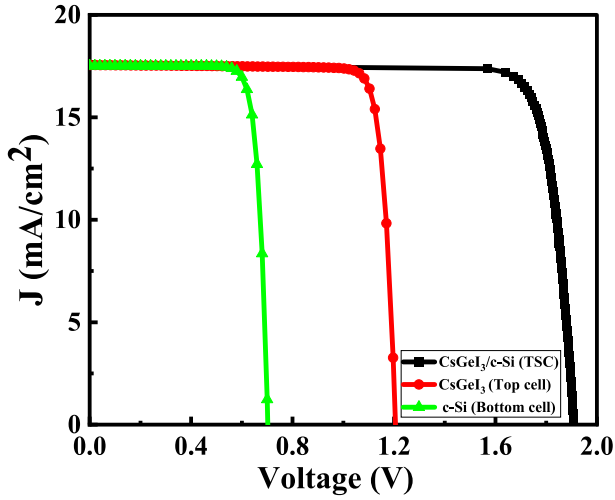


Fig. 18. J-V curve of studied CsGeI<sub>3</sub>-on-c-Si TSC with current matching of T&B cell.

**Table 4**  
Summary of PV parameters extracted from SCAPS 1D simulation.

Structures	V <sub>oc</sub> (V)	J <sub>sc</sub> (mA/cm <sup>2</sup> )	FF (%)	PCE (%)
Top cell CsGeI <sub>3</sub> (265 nm)	1.20	17.55	86.4	18.31
Bottom cell c-Si(400 μm) under filtered spectrum	0.70	17.50	82.62	10.15
CsGeI <sub>3</sub> /c-Si tandem device	1.90	17.55	84.90	28.43

**Table 5**  
Experimental and Simulation Results of PV parameters of different PVSK/Si TSCs.

SC architectures	V <sub>oc</sub> (V)	J <sub>sc</sub> (mA/cm <sup>2</sup> )	FF (%)	PCE (%)
Cu <sub>2</sub> ZnSn(S,Se) <sub>4</sub> /CIGS, Experimental [82]	1.45	16.1	68.2	15.9
FA <sub>0.75</sub> Cs <sub>0.25</sub> Pb(I <sub>0.8</sub> Br <sub>0.2</sub> ) <sub>3</sub> /Si, Experimental [83]	1.77	18.4	77	25
Perovskite/Si, Experimental [84]	1.65	16.5	81.1	22.22
CsPbI <sub>3</sub> /Si, Experimental [85]	1.23	13.47	0.65	10.77
Cs <sub>2</sub> AgBi <sub>0.75</sub> Sb <sub>0.25</sub> Br <sub>6</sub> /Si, Simulation [86]	1.76	16.01	86.7	24.4
CH <sub>3</sub> NH <sub>3</sub> PbI <sub>3</sub> /Si, Simulation [87]	1.77	20.19	82.22	28.50
Cs <sub>2</sub> AgBi <sub>0.75</sub> Sb <sub>0.25</sub> Br <sub>6</sub> /Si, Simulation [88]	1.76	43.13	86.70	24.40
CsGeI <sub>3</sub> /c-Si (This work)	1.90	17.55	84.9	28.43

decreases with rising temperature due to the increase in  $n_i$ , which increases the dark saturation current. The intrinsic carrier density is related to the  $E_g$  of the semiconductor materials and the ambient temperature. The relation between the  $E_g$ , carrier density and temperature is given by equations (13) and (14) [68,88].

$$n_i^2 = a e^{\frac{E_g}{kT}} \quad (13)$$

$$E_g(T) = E_g(0) - \frac{aT^2}{T+b} \quad (14)$$

where T is temperature,  $E_g(T)$  is the temperature dependent  $E_g$  and a and b are constants.

## 5.2. Modelling approaches for CsGeI<sub>3</sub>/c-Si tandem device

To validate the findings of our simulated results of CsGeI<sub>3</sub>-on-c-Si

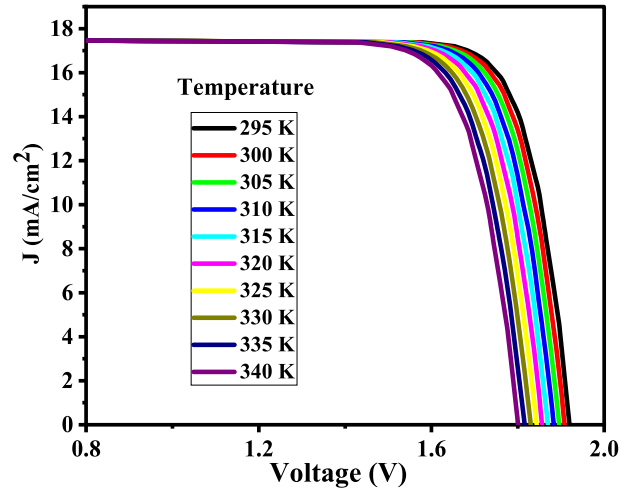


Fig. 19. J-V characteristics performance of CsGeI<sub>3</sub>/Si TSC with respect to temperature variation.

TSC, we employed the semi-analytical equations of the circuit model of a two terminal TSC composed of two series-connected diodes, as shown in Fig. 20 (a). For a single junction SC, we may write the current density-voltage equation as [89].

$$J(V) = J_{ph} - J_{0,eff} \left[ \exp \left( \frac{V + J(V)R_s}{AV_{TH}} \right) \right] - \frac{V + J(V)R_s}{R_{sh}} \quad (15)$$

where  $J_{ph}$  is the photo current density,  $J_0$  denotes the dark current density, A is the photodiode diode ideality factor,  $V_{th}$  is the thermal voltage,  $R_{sh}$  and  $R_s$  are the shunt and series resistances per unit area respectively. Eq (11) is used to compute the J-V characteristics of both the top cell (CsGeI<sub>3</sub>) and the bottom cell (c-Si). It is assumed that the value of  $J_{ph}$  for both the T&B cells will be equivalent to the value of  $J_{sc}$  that was obtained from the simulations. In order to compute the values of  $R_{sh}$  and  $R_s$ , we have adopted the procedure as described. The modified version of the J-V plot of the PV cells can be represented as given below [90]:

$$J = J_{sc}(1 - yV^x) - g_d V \quad (16) \text{ where } x, y \text{ and } g_d \text{ are the model parameters computed using the expressions given below [89,90]:}$$

$$g_d = \frac{(J_{sc} - J_2)}{V_2} \quad (17)$$

$$x = \frac{\log[(J_{sc} - g_d V_{oc})/(J_{sc} - J_1 - g_d V_1)]}{\log(V_{oc}/V_1)} \quad (18)$$

$$y = \frac{(V_2 - V_1)J_{sc} - V_2J_1 + V_1J_2}{J_{sc}V_1V_2(V_1^{x-1} - V_2^{x-1})} \quad (19)$$

( $J_1, V_1$ ) and ( $J_2, V_2$ ) the current and voltage values at (0.72  $J_{sc}$ ,  $V_{oc}$ ) and ( $J_{sc}$ , 0.3 $V_{oc}$ ) respectively as depicted in Fig. 20 (b).  $R_s$  and parasitic  $R_{sh}$  are determined using the equations given below:

$$R_s = - \left( \frac{dV}{dJ} \right)_{J=0} = \frac{1}{(g_d + xyJ_{sc}V_{oc}^{x-1})} \quad (20)$$

$$R_{sh} = - \left( \frac{dV}{dJ} \right)_{V=0} = \frac{1}{g_d} \quad (21)$$

The performance parameters of the sub-cells computed from the semi-analytical model, and simulations are listed in Table 6. The different PV parameters for the two sub-cells  $A_i$ ,  $J_{0,i}$ ,  $R_{s,i}$  and  $R_{sh,i}$  ( $i = 1$  for top cell and 2 for bottom cell) are used to compute the overall parameters for the TSC as listed below [91]:

$$J_1(V_1) = J_2(V_1) = J_2(V_1 + V_2) = J(V) \quad (22)$$



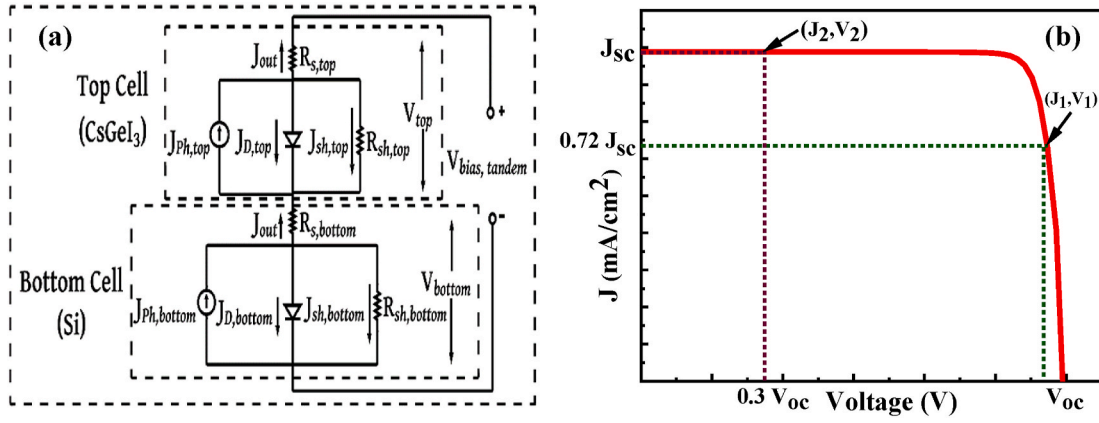


**Fig. 20.** (a) Equivalent circuit diagram of a CsGeI<sub>3</sub>/Si TSC consisting of two diodes in series connection.  $J_{out}$  is the output current and  $V_{bias}$  is the output voltage and (b) J-V curve of SC for obtaining of the biasing points utilizing the values of  $J_{sc}$  and  $V_{oc}$ .

**Table 6**

The parameters of sub cells obtained from semi-analytical model.

Parameters	A	$g_d$ ( $m\Omega^{-1}$ )	$x$	$y$ (1/V)	$R_s$ ( $\Omega/cm^2$ )	$R_{sh}$ ( $\Omega/cm^2$ )	$V_{oc}$ (V)	$J_{sc}$ (mA/cm <sup>2</sup> )	FF (%)	PCE (%)
Top cell	1.3	0.097	25.1	0.01	1.4	$1 \times 10^4$	1.2	17.6	86.65	18.2
Bottom cell	1.2	0.095	17.3	474.8	2.1	$1 \times 10^4$	0.7	17.5	82.18	10.1
Tandem	–	–	–	–	–	–	1.9	17.6	84.6	28.4

$$V = \sum_{i=1,2} V_i = V_1 + V_2 \quad (23)$$

$$A_{s,eff} = \sum_{i=1,2} A_i = A_1 + A_2 \quad (24)$$

$$R_{s,eff} = \sum_{i=1,2} R_{s,i} = R_{s,1} + R_{s,2} \quad (25)$$

$$J_{0,eff} = \prod_{i=1,2} J_{0,i}^{A_i/A_{eff}} = J_{0,i}^{A_i/A_{eff}} J_{0,i}^{A_i/A_{eff}} \quad (26)$$

$$R_{s,eff} = \sum_{i=1,2} R_{sh,i} = R_{sh,1} + R_{sh,2}$$

J-V equation of the TSC can be written as follows [91]:

$$J(V) = J_{ph,eff} - J_{0,eff} \left[ \exp \left( \frac{V + J(V)R_{s,eff}}{a_{eff}} \right) - \frac{V + J(V)R_{s,eff}}{R_{sh,eff}} \right] \quad (27)$$

The J-V curve of the simulation and the model for the CsGeI<sub>3</sub> and Si-based sub-cells are shown in Fig. 21. Along with the plot of the TSC that was obtained by applying Eq (27), it can be seen that a close match exists between the obtained simulation results and the results achieved using semi-analytical model.

## 6. Conclusions

In this work, the photovoltaic performance of a two-terminal CsGeI<sub>3</sub>/c-Si TSC has been explored through a detailed and systematic investigation of the optoelectronic properties of lead-free CsGeI<sub>3</sub> using DFT framework and using these computed properties for the examination of PV parameters of the proposed SC with SCAPS 1D simulation. Additionally, in our model, we employed the assumption of ideal current matching conditions, which implies negligible recombination and absorption losses at the Interfacial Charge Layer (ICL). While this is a simplifying assumption commonly adopted in solar cell modeling, it is crucial to acknowledge that ideal ICL conditions may lead to an overestimation of the solar cell's performance. Despite this limitation, the use of this assumption remains a valuable tool in solar cell modeling. It

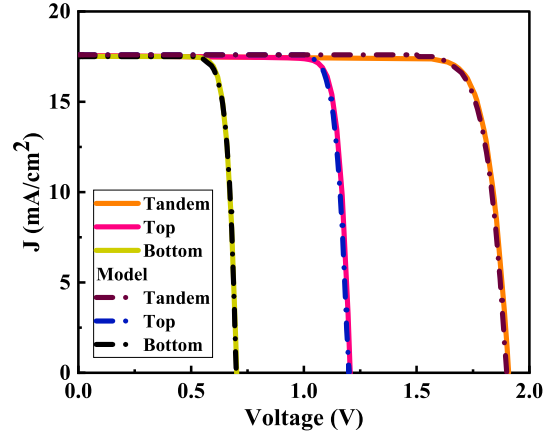


**Fig. 21.** J-V curve of the studied CsGeI<sub>3</sub>-on-c-Si TSC and standalone bottom and top cells with current matching using SCAPS-1D (Solid line) and semi-analytical model (dashed line).

aids in pinpointing the critical factors influencing the solar cell's performance and in devising strategies to improve its design. However, for future research endeavors, a comprehensive investigation into the impact of non-ideal ICL conditions on the proposed device's performance is warranted. The main highlights of this theoretical investigation can be summarized as follows.

1. DFT calculations predict that CsGeI<sub>3</sub> possesses a direct  $E_g$  value of 1.6 eV, which is close to the reported experimental and theoretical values. CsGeI<sub>3</sub> is suitable for PV applications as it shows good absorption in the visible region and exhibits worthy photoelectric properties in addition to being non-toxic. From the DOS plot, it is evident that Ge and I atoms (major) contribute to the VB states and Cs and I atoms contribute to the energy states in the CB.
2. For the simulation of TSC, the filtered spectrum transmitted from top CsGeI<sub>3</sub> cell is incident on the bottom c-Si SC, and the current matching process is carried out through a variation of the thickness of the absorber layers of both the bottom, and top SCs. Both the

bottom and top cells are calibrated with experimental data in order to make the simulations realistic. Thereafter the performance of the CsGeI<sub>3</sub> top cell is optimized in order to achieve enhanced performance.

3. The effect of  $R_s$  and  $R_{sh}$  and the interfacial and bulk defects in the absorber layer of the top cell are analysed in detail for the optimization of the performance. From this analysis, it is established that both  $V_{oc}$  and  $J_{sc}$  remains almost constant for  $R_{sh}$  beyond  $100 \Omega\text{-cm}^2$  whereas the PCE and FF initially increases  $R_{sh}$  up to  $10^4 \Omega\text{-cm}^2$  but saturates beyond this value of  $R_{sh}$ . From the  $N_t$  analysis, it can be noted that both interfacial and bulk defects deteriorated the PV performance. Interface  $N_t$  has the stronger effects on  $J_{sc}$  and the tolerable limit of interface  $N_t$  can be considered up to  $10^{14} \text{cm}^{-2}$ .
4. CsGeI<sub>3</sub>/Si TSC delivered a PCE of 28.43 % with  $J_{sc}$  of  $17.55 \text{mA/cm}^2$ ,  $V_{oc}$  of 1.90 V and FF of 84.90 % under current matching condition. For an absorber layer thickness of 265 nm and 400  $\mu\text{m}$  respectively, the standalone T&B cells exhibited PCE of 18.31 % and 10.15 % respectively.
5. A semi-analytical model based on an equivalent circuit model of two series connected diodes is used to compute the PV parameters and intrinsic resistances analytically and it is found that there exists a close match between the simulated and analytically computed results.

Thus, this in-depth analysis of PVSK-on-Si TSC architecture will open new horizons for the realization of cheap and efficient PVSK based TSC architectures that can compete with the existing costly inorganic multijunction SCs.

## Declaration

The authors declare explicitly that they have no financial, personal, or other relationships with any third parties that may be seen as having influenced the work reported in this research.

## CRediT authorship contribution statement

**Babban Kumar Ravidas:** Writing – original draft, Validation, Software, Methodology, Investigation, Formal analysis. **Abhijit Das:** Validation, Software, Investigation. **Suneet Kumar Agnihotri:** Visualization, Validation, Formal analysis. **Rahul Pandey:** Writing – review & editing, Visualization, Formal analysis. **Jaya Madan:** Writing – review & editing, Visualization, Formal analysis. **M. Khalid Hossain:** Writing – review & editing, Visualization, Formal analysis. **Mukesh Kumar Roy:** Writing – review & editing, Visualization, Supervision, Resources, Investigation. **D.P. Samajdar:** Writing – review & editing, Supervision, Project administration, Investigation, Formal analysis, Conceptualization.

## Declaration of competing interest

The authors declare the following financial interests/personal relationships which may be considered as potential competing interests.

## Data availability

No data was used for the research described in the article.

## Acknowledgements

This work is funded by the Scheme for Transformational and Advanced Research in Sciences (STARS) Ministry of Education, Government of India and implemented, monitored and managed by Indian Institute of Science (IISc), Bangalore vide Grant No. MoE-STARS/STARS-2/2023-0401.

The authors are thankful to Prof. M. Burgelman, Department of

Electronics and Information Systems, University of Gent, for offering the access of SCAPS-1D.

## References

- [1] L. Hammarström, Overview: capturing the sun for energy production, *Ambio* 41 (2012) 103–107.
- [2] I. Çelik, A. Phillips, Z. Song, Y. Yan, R. Ellingson, M. Heben, D. Apul, Environmental analysis of perovskites and other relevant solar cell technologies in a tandem configuration, *Energy Environ. Sci.* 10 (2017).
- [3] M.K. Hossain, D.P. Samajdar, R.C. Das, A.A. Arnab, M.F. Rahman, M.H.K. Rubel, M. R. Islam, H. Bencherif, R. Pandey, J. Madan, M.K.A. Mohammed, Design and simulation of Cs<sub>2</sub>BiAgI<sub>6</sub> double perovskite solar cells with different electron transport layers for efficiency enhancement, *Energy & Fuels* 37 (2023) 3957–3979.
- [4] A. Kojima, K. Teshima, Y. Shirai, T. Miyasaka, Organometal halide perovskites as visible-light sensitizers for photovoltaic cells, *J. Am. Chem. Soc.* 131 (2009) 6050–6051.
- [5] T. Dureja, A. Garg, S. Bhalla, D. Bhutani, A. Khanna, Double lead-free perovskite solar cell for 19.9% conversion efficiency: a SCAPS-1D based simulation study, *Mater. Today: Proc.* 71 (2022) 239–242.
- [6] J. Wu, Y. Li, Y. Li, W. Xie, J. Shi, D. Li, S. Cheng, Q. Meng, Using hysteresis to predict the charge recombination properties of perovskite solar cells, *J. Mater. Chem. A* 9 (2021) 6382–6392.
- [7] T. Ameri, N. Li, C.J. Brabec, Highly efficient organic tandem solar cells: a follow up review, *Energy Environ. Sci.* 6 (2013) 2390–2413.
- [8] A. Richter, M. Hermle, S.W. Glunz, Reassessment of the limiting efficiency for crystalline silicon solar cells, *IEEE J. Photovoltaics* 3 (2013) 1184–1191.
- [9] Z. Zhu, X. Jiang, D. Yu, N. Yu, Z. Ning, Q. Mi, Smooth and compact FASnI<sub>3</sub> films for lead-free perovskite solar cells with over 14% efficiency, *ACS Energy Lett.* 7 (2022) 2079–2083.
- [10] M. Sulaman, S.Y. Yang, Z.H. Zhang, A. Imran, A. Bukhtiar, Z.H. Ge, Y. Tang, Y. R. Jiang, L.B. Tang, B.S. Zou, Lead-free tin-based perovskites nanocrystals for high-performance self-driven bulk-heterojunction photodetectors, *Materials Today Physics* 27 (2022) 100829.
- [11] W. Ming, H. Shi, M.-H. Du, Large dielectric constant, high acceptor density, and deep electron traps in perovskite solar cell material CsGeI<sub>3</sub>, *J. Mater. Chem. A* 4 (2016) 13852–13858.
- [12] A. Tara, V. Bharti, S. Sharma, R. Gupta, Computational approach to explore suitable charge transport layers for all inorganic CsGeI<sub>3</sub> perovskite solar cells, *Opt. Mater.* 128 (2022) 112403.
- [13] T. Krishnamoorthy, H. Ding, C. Yan, W.L. Leong, T. Baikie, Z. Zhang, M. Sherburne, S. Li, M. Asta, N. Mathews, Lead-free germanium iodide perovskite materials for photovoltaic applications, *J. Mater. Chem. A* 3 (2015) 23829–23832.
- [14] J. Qian, B. Xu, W. Tian, A comprehensive theoretical study of halide perovskites ABX<sub>3</sub>, *Org. Electron.* 37 (2016) 61–73.
- [15] L.-J. Chen, Synthesis and optical properties of lead-free cesium germanium halide perovskite quantum rods, *RSC Adv.* 8 (2018) 18396–18399.
- [16] N. Liu, L. Wang, F. Xu, J. Wu, T. Song, Q. Chen, Recent progress in developing monolithic perovskite/Si tandem solar cells, *Front. Chem.* 8 (2020) 603375.
- [17] P. Löper, B. Niesen, S.J. Moon, S.M.d. Nicolas, J. Holovsky, Z. Remes, M. Ledinsky, F.J. Haug, J.H. Yum, S.D. Wolf, C. Ballif, Organic–inorganic halide perovskites: perspectives for silicon-based tandem solar cells, *IEEE J. Photovoltaics* 4 (2014) 1545–1551.
- [18] M. Azadnia, M. Ameri, R.T. Ghahrizjani, M. Fathollahi, Maximizing the performance of single and multijunction MA and lead-free perovskite solar cell, *Mater. Today Energy* 20 (2021) 100647.
- [19] J. Madan, Shivani, R. Pandey, R. Sharma, Device simulation of 17.3% efficient lead-free all-perovskite tandem solar cell, *Sol. Energy* 197 (2020) 212–221.
- [20] A. Das, S.D. Peu, M.A.M. Akanda, M.M. Salah, M.S. Hossain, B.K. Das, Numerical simulation and optimization of inorganic lead-free Cs<sub>3</sub>Bi<sub>2</sub>I<sub>9</sub>-based perovskite photovoltaic cell: impact of various design parameters, *Energies* 16 (2023) 2328.
- [21] S. Abdelaziz, A. Zekry, A. Shaker, M. Abouelatta, Investigation of lead-free MASnI<sub>3</sub>-MASnI<sub>3</sub>Br<sub>2</sub> tandem solar cell: numerical simulation, *Opt. Mater.* 123 (2022) 111893.
- [22] S.S.I. Almishal, O. Rashwan, A comparative study of the structural and electronic properties of orthorhombic and cubic CsPbI<sub>3</sub> and trigonal CsGeI<sub>3</sub> using first-principles calculations, in: 2021 IEEE 48th Photovoltaic Specialists Conference, (PVSC), 2021, pp. 1837–1841.
- [23] S. Idrissi, S. Ziti, H. Labrim, L. Bahmad, Band gaps of the solar perovskites photovoltaic CsXCl<sub>3</sub> (X=Sn, Pb or Ge), *Mater. Sci. Semicond. Process.* 122 (2021) 105484.
- [24] M. Houari, B. Bouadjemi, M. Matougui, S. Haid, T. Lantri, Z. Aziz, S. Bentata, B. Bouhafs, Optoelectronic properties of germanium iodide perovskites AgI<sub>3</sub> (A = K, Rb and Cs): first principles investigations, *Opt. Quant. Electron.* 51 (2019) 234.
- [25] L. Magnani, N. Nersessian, N.J. Nersessian, L. Magnani, Model-based Reasoning: Science, Technology, Values, Springer Science & Business Media, 2002.
- [26] A. Slami, Numerical Study of Based Perovskite Solar Cells by SCAPS-1D, 2019.
- [27] A.C. Piñón Reyes, R.C. Ambrosio Lázaro, K. Monfil Leyva, J.A. Luna López, J. Flores Méndez, A.H. Heredia Jiménez, A.L. Muñoz Zurita, F. Severiano Carrillo, E. Ojeda Durán, Study of a lead-free perovskite solar cell using CZTS as HTL to achieve a 20% PCE by SCAPS-1D simulation, *Micromachines* 12 (2021) 1508.
- [28] K. Deepthi Jayan, Design and comparative performance analysis of high-efficiency lead-based and lead-free perovskite solar cells, *Phys. Status Solidi* 219 (2022) 2100606.

- [29] H. Son, B.-S. Jeong, Optimization of the power conversion efficiency of CsPbI<sub>3</sub>Br<sub>3</sub>-x-based perovskite photovoltaic solar cells using ZnO and NiO<sub>x</sub> as an inorganic charge transport layer, *Appl. Sci.* 12 (2022) 8987.
- [30] B.K. Ravidas, M.K. Roy, D.P. Samajdar, Investigation of photovoltaic performance of lead-free CsSnI<sub>3</sub>-based perovskite solar cell with different hole transport layers: first Principle Calculations and SCAPS-1D Analysis, *Sol. Energy* 249 (2023) 163–173.
- [31] A. Thakur, D. Singh, S. Kaur Gill, Numerical simulations of 26.11% efficient planar CH<sub>3</sub>NH<sub>3</sub>PbI<sub>3</sub> perovskite n-i-p solar cell, *Mater. Today: Proc.* 71 (2022) 195–201.
- [32] M. Taguchi, A. Yano, S. Tohoda, K. Matsuyama, Y. Nakamura, T. Nishiwaki, K. Fujita, E. Maruyama, 24.7% record efficiency HIT solar cell on thin silicon wafer, *IEEE J. Photovoltaics* 4 (2014) 96–99.
- [33] G. Pindolia, S. Shinde, P. Jha, Optimization of an inorganic lead free RbGeI<sub>3</sub> based perovskite solar cell by SCAPS-1D simulation, *Sol. Energy* (2022) 236.
- [34] F.M. Rombach, S.A. Haque, T.J. Macdonald, Lessons learned from spiro-OMeTAD and PTAA in perovskite solar cells, *Energy Environ. Sci.* 14 (2021) 5161–5190.
- [35] D. Saikia, J. Bera, A. Betal, S. Sahu, Performance evaluation of an all inorganic CsGeI<sub>3</sub> based perovskite solar cell by numerical simulation, *Opt. Mater.* 123 (2022) 111839.
- [36] P. Sawicka-Chudy, Z. Starowicz, G. Wysz, R. Yavorskyi, Z. Zapukhyak, M. Bester, M. Sibiński, M. Cholewa, Simulation of TiO<sub>2</sub>/CuO solar cells with SCAPS-1D software, *Mater. Res. Express* 6 (2019) 085918.
- [37] L. Usgodaarachchi, C. Thambiliyagodage, R. Wijesekera, S. Vigneswaran, M. Kandanapitiye, Fabrication of TiO<sub>2</sub> spheres and a visible light active  $\alpha$ -Fe<sub>2</sub>O<sub>3</sub>/TiO<sub>2</sub>-rutile/TiO<sub>2</sub>-anatase heterogeneous photocatalyst from natural ilmenite, *ACS Omega* 7 (2022) 27617–27637.
- [38] D. Stanić, V. Kojić, T. Čizmar, J. Krunoslav, L. Bagladi, J. Mangalam, T. Rath, A. Gajović, Simulating the Performance of a Formamidinium Based Mixed Cation Lead Halide Perovskite Solar Cell, 2021.
- [39] L. Kerkache, A. Layadi, E. Dogheche, D. Remiens, Physical properties of RF sputtered TiO thin films and annealing effect, *J. Phys. Appl. Phys.* 39 (2005) 184.
- [40] A. Halal, A.I. Alnahhal, B. Plesz, Numerical simulation and design optimization of highly efficient lead-free perovskite/c-Si tandem solar cell, in: 2022 22nd International Scientific Conference on Electric Power Engineering, (EPE), 2022, pp. 1–6.
- [41] J. Liang, E.A. Schiff, S. Guha, B. Yan, J. Yang, Hole-mobility limit of amorphous silicon solar cells, *Appl. Phys. Lett.* 88 (2006).
- [42] C. Battaglia, A. Cuevas, S. De Wolf, High-efficiency crystalline silicon solar cells: status and perspectives, *Energy Environ. Sci.* 9 (2016) 1552–1576.
- [43] N. Shrivastav, J. Madan, R. Pandey, A.E. Shalan, Investigations aimed at producing 33% efficient perovskite-silicon tandem solar cells through device simulations, *RSC Adv.* 11 (2021) 37366–37374.
- [44] M.S.S. Basyoni, M.M. Salah, M. Mousa, A. Shaker, A. Zekry, M. Abouelatta, M. T. Alshammari, K.A. Al-Dhlan, C. Gontrand, On the investigation of interface defects of solar cells: lead-based vs lead-free perovskite, *IEEE Access* 9 (2021) 130221–130232.
- [45] Y. He, L. Xu, C. Yang, X. Guo, S. Li, Design and Numerical Investigation of a Lead-Free Inorganic Layered Double Perovskite Cs<sub>4</sub>CuSb<sub>2</sub>(2)Cl<sub>12</sub> Nanocrystal Solar Cell by SCAPS-1D, *Nanomaterials*, Basel, Switzerland, 2021, p. 11.
- [46] A.A.B. Baloch, M.I. Hossain, N. Tabet, F.H. Alharbi, Practical efficiency limit of Methylammonium lead iodide perovskite (CH<sub>3</sub>NH<sub>3</sub>PbI<sub>3</sub>) solar cells, *J. Phys. Chem. Lett.* 9 (2018) 426–434.
- [47] S. Sarker, M.T. Islam, A. Rauf, H. Al Jame, M.R. Jani, S. Ahsan, M.S. Islam, S. S. Nishat, K.M. Shorowordi, S. Ahmed, A SCAPS simulation investigation of non-toxic MAGEI<sub>3</sub>-on-Si tandem solar device utilizing monolithically integrated (2-T) and mechanically stacked (4-T) configurations, *Sol. Energy* 225 (2021) 471–485.
- [48] M. Filipić, P. Löper, B. Niesen, S. De Wolf, J. Krč, C. Ballif, M. Topić, CH<sub>3</sub>NH<sub>3</sub>PbI<sub>3</sub> perovskite/silicon tandem solar cells: characterization based optical simulations, *Opt Express* 23 (2015) A263–A278.
- [49] Y. Cheng, L. Ding, Perovskite/Si tandem solar cells: fundamentals, advances, challenges, and novel applications, *SusMat* 1 (2021) 324–344.
- [50] M.T. Islam, M.R. Jani, A.F. Islam, K.M. Shorowordi, S. Chowdhury, S.S. Nishat, S. Ahmed, Investigation of CsSn 0.5 Ge 0.5 I 3-on-Si tandem solar device utilizing SCAPS simulation, *IEEE Trans. Electron. Dev.* 68 (2021) 618–625.
- [51] H.M. Ghaithan, Z.A. Alahmed, S.M.H. Qaid, A.S. Aldwayyan, Density functional theory analysis of structural, electronic, and optical properties of mixed-halide orthorhombic inorganic perovskites, *ACS Omega* 6 (2021) 30752–30761.
- [52] C.S. Baird, *Absorption of Electromagnetic Radiation*, McGraw Hill, New York, 2019.
- [53] L.-K. Gao, Y.-L. Tang, X.-F. Diao, First-Principles study on the photoelectric properties of CsGeI<sub>3</sub> under hydrostatic pressure, *Appl. Sci.* 10 (2020) 5055.
- [54] K. Ephraim Babu, A. Veeraiyah, D. Tirupathi Swamy, V. Veeraiyah, First-principles study of electronic and optical properties of cubic perovskite CsSrF<sub>3</sub>, *Materials Science-Poland* 30 (2012) 359–367.
- [55] D. Adachi, J.L. Hernandez, K. Yamamoto, Impact of carrier recombination on fill factor for large area heterojunction crystalline silicon solar cell with 25.1% efficiency, *Appl. Phys. Lett.* 107 (2015) 233506.
- [56] D. Saikia, J. Bera, A. Betal, S.J.O.M. Sahu, Performance evaluation of an all inorganic CsGeI<sub>3</sub> based perovskite solar cell by numerical simulation 123 (2022) 111839.
- [57] E. Akoto, V. Isahi, V. Odari, C. Maghanga, F.J.R.I.O. Nyongesa, Monolith Cs<sub>1-x</sub>Rb<sub>x</sub>SnI<sub>3</sub> perovskite-silicon 2T tandem solar cell using, SCAPS-1D 12 (2023) 100470.
- [58] S. Abdelaziz, A. Zekry, A. Shaker, M.J.O.M. Abouelatta, Investigation of lead-free MASnI<sub>3</sub>-MASnBr<sub>2</sub> tandem solar cell, *Numerical simulation* 123 (2022) 111893.
- [59] S. Albrecht, M. Saliba, J.P. Correa Baena, F. Lang, L. Kegelmann, M. Mews, L. Steier, A. Abate, J. Rappich, L. Korte, R. Schlattmann, M.K. Nazeeruddin, A. Hagfeldt, M. Grätzel, B. Rech, Monolithic perovskite/silicon-heterojunction tandem solar cells processed at low temperature, *Energy Environ. Sci.* 9 (2016) 81–88.
- [60] K.A. Bush, A.F. Palmstrom, Z.J. Yu, M. Boccard, R. Cheacharoen, J.P. Mailoa, D. P. McMeekin, R.L.Z. Hoyer, C.D. Bailie, T. Leijtens, I.M. Peters, M.C. Minichetti, N. Rolston, R. Prasanna, S. Sofia, D. Harwood, W. Ma, F. Moghadam, H.J. Snaith, T. Buonassisi, Z.C. Holman, S.F. Bent, M.D. McGehee, 23.6%-efficient monolithic perovskite/silicon tandem solar cells with improved stability, *Nat. Energy* 2 (2017) 17009.
- [61] K. Datta, B. Branco, Y. Zhao, V. Zardetto, N. Phung, A. Bracesco, L. Mazzarella, M. M. Wient, M. Creatore, O. Isabella, R.A.J. Janssen, Efficient continuous light-driven electrochemical water splitting enabled by monolithic perovskite-silicon, *Tandem Photovoltaics* 8 (2023) 2201131.
- [62] P.J.S. Caprioglio, perovskiteMonolithic/silicon tandem solar cell with > 29% efficiency by enhanced hole extraction 370 (2020) 1300–1309.
- [63] A.J. Bett, P.S. Schulze, K.M. Winkler, Ö.S. Kabakli, I. Ketterer, L.E. Mundt, S. K. Reichmuth, G. Siefer, L. Tutsch, Two-terminal Perovskite silicon tandem solar cells with a high-Bandgap Perovskite absorber enabling voltages over 1.8 V, *Prog. Photovoltaics Res. Appl.* 28 (2020) 99–110.
- [64] M. De Bastiani, E. Van Kerschaver, Q. Jeangros, A. Ur Rehman, E. Aydin, F. H. Isikgor, A.J. Mirabelli, M. Babics, J. Liu, S.J.A.E.L. Zhumagali, Toward stable monolithic perovskite/silicon tandem photovoltaics: a six-month outdoor performance study in a hot and humid climate 6 (2021) 2944–2951.
- [65] B. Marteau, T. Desrués, Q. Rahay, A. Kaminski, S. Dubois, Passivating silicon tunnel diode for perovskite on silicon nip tandem solar cells, *Energies* 16 (2023) 4346.
- [66] Y. Cheng, L. Ding, Perovskite/Si tandem solar cells: fundamentals, advances, challenges, and novel applications 1 (2021) 324–344.
- [67] A.F. Palmstrom, G.E. Eperon, T. Leijtens, R. Prasanna, S.N. Habisreutinger, W. Nemeth, E.A. Gaubling, S.P. Dunfield, M. Reese, S. Nanayakkara, T. Moot, J. Werner, J. Liu, B. To, S.T. Christensen, M.D. McGehee, M.F.A.M. van Hest, J. M. Luther, J.J. Berry, D.T. Moore, Enabling flexible all-perovskite tandem solar cells, *Joule* 3 (2019) 2193–2204.
- [68] M.K. Hossain, G.F.I. Toki, I. Alam, R. Pandey, D.P. Samajdar, M.F. Rahman, M. R. Islam, M.H.K. Rubel, H. Bencherif, J. Madan, M.K.A. Mohammed, Numerical simulation and optimization of a CsPbI<sub>3</sub>-based perovskite solar cell to enhance the power conversion efficiency, *New J. Chem.* 47 (2023) 4801–4817.
- [69] M.T. Islam, M.R. Jani, A.F. Islam, K.M. Shorowordi, S. Chowdhury, S.S. Nishat, S. Ahmed, Investigation of CsSn<sub>0.5</sub>Ge<sub>0.5</sub>I<sub>3</sub>-on-Si tandem solar device utilizing SCAPS simulation, *IEEE Trans. Electron. Dev.* 68 (2021) 618–625.
- [70] K. Ghosh, C.J. Tracy, S. Herasimenka, C. Honsberg, S. Bowden, Explanation of the device operation principle of amorphous silicon/crystalline silicon heterojunction solar cell and role of the inversion of crystalline silicon surface, in: 2010 35th IEEE Photovoltaic Specialists Conference, IEEE, 2010, pp. 1383–1386.
- [71] Y. Tsunomura, Y. Yoshimine, M. Taguchi, T. Baba, T. Kinoshita, H. Kanno, H. Sakata, E. Maruyama, M. Tanaka, Twenty-two percent efficiency HIT solar cell, *Sol. Energy Mater. Sol. Cell.* 93 (2009) 670–673.
- [72] U. Mandadapu, V. Vedanayakam, K. Thyagarajan, Simulation and analysis of lead based perovskite solar cell using SCAPS-1D, *Indian J. Sci. Technol.* 10 (2017) 1–8.
- [73] S. Porwal, M. Paul, H. Dixit, S. Mishra, T. Singh, Investigation of defects in Cs<sub>2</sub>Ni<sub>6</sub>-based double perovskite solar cells via SCAPS-1D, *Advanced Theory and Simulations* 5 (2022) 2200207.
- [74] M. Jiang, J. Tang, Simulated development and optimized performance of narrow-bandgap CsSnI<sub>3</sub>-based all-inorganic perovskite solar cells, *J. Phys. Appl. Phys.* 54 (2021) 465104.
- [75] S. Taheri, M. Minbashi, A. Hajjiah, Effect of defects on high efficient perovskite solar cells, *Opt. Mater.* 111 (2021) 110601.
- [76] M. Islam, M. Jani, A. Islam, M. S. S. Chowdhury, S. Nishat, S. Ahmed, Investigation of CsSn<sub>0.5</sub>Ge<sub>0.5</sub>I<sub>3</sub>-On-Si Tandem Solar Device Utilizing SCAPS Simulation, *IEEE Transactions on Electron Devices*, 2021, pp. 1–8.
- [77] A. Sunny, S. Rahman, M.M. Khatun, S.R.A. Ahmed, Numerical study of high performance HTL-free CH<sub>3</sub>NH<sub>3</sub>SnI<sub>3</sub>-based perovskite solar cell by SCAPS-1D, *AIP Adv.* 11 (2021) 065102.
- [78] H. Krawiec, J. Lelito, M. Mróz, M. Radoń, Influence of heat treatment parameters of austempered ductile iron on the microstructure, *Corrosion and Tribological Properties* 16 (2023) 4107.
- [79] Z. Yu, I.R. Perera, T. Daenke, S. Makuta, Y. Tachibana, J.J. Jasieniak, A. Mishra, P. Bäuerle, L. Spiccia, U. Bach, Indium tin oxide as a semiconductor material in efficient p-type dye-sensitized solar cells, *NPG Asia Mater.* 8 (2016) e305, e305.
- [80] I.J. Park, H.K. An, Y. Chang, J.Y. Kim, Interfacial modification in perovskite-based tandem solar cells, *Nano Convergence* 10 (2023) 22.
- [81] S.R. Hosseini, M. Bahramgour, P.Y. Sefidi, A.T. Mashayekh, A. Moradi, N. Delibas, M.G. Hosseini, A.J.H. Niaei, Investigating the Effect of Non-ideal Conditions on the Performance of a Planar CH<sub>3</sub>NH<sub>3</sub>PbI<sub>3</sub>-based Perovskite Solar Cell through SCAPS-1D Simulation, vol. 8, 2022.
- [82] T. Todorov, T. Gershon, O. Gunawan, Y.S. Lee, C. Sturdevant, L.Y. Chang, S. Guha, Monolithic perovskite-CIGS tandem solar cells via in situ band gap engineering, *Adv. Energy Mater.* 5 (2015) 1500799.
- [83] K.A. Bush, S. Manzoor, K. Frohna, Z.J. Yu, J.A. Raiford, A.F. Palmstrom, H.-P. Wang, R. Prasanna, S.F. Bent, Z.C. Holman, Minimizing current and voltage losses to reach 25% efficient monolithic two-terminal perovskite-silicon tandem solar cells, *ACS Energy Lett.* 3 (2018) 2173–2180.

- [84] Z. Qiu, Z. Xu, N. Li, N. Zhou, Y. Chen, X. Wan, J. Liu, N. Li, X. Hao, P. Bi, Q. Chen, B. Cao, H. Zhou, Monolithic perovskite/Si tandem solar cells exceeding 22% efficiency via optimizing top cell absorber, *Nano Energy* 53 (2018) 798–807.
- [85] W. Ahmad, J. Khan, G. Niu, J. Tang, Inorganic CsPbI<sub>3</sub> perovskite-based solar cells: a choice for a tandem device, *Sol. RRL* 1 (2017) 1700048.
- [86] N.N. Lal, Y. Dkhissi, W. Li, Q. Hou, Y.B. Cheng, U. Bach, Perovskite tandem solar cells, *Adv. Energy Mater.* 7 (2017) 1602761.
- [87] A.D. Afrasiab, F.E. Khan, A.D. Subhan, S.D. Khan, M.S. Khan, Ahmad, S. M, M. Rehan, Noman, Optimization of efficient monolithic perovskite/silicon tandem solar cell, *Optik* 208 (2020) 164573.
- [88] K. Amri, R. Belghouthi, M. Aillerie, R. Gharbi, Device optimization of a lead-free perovskite/silicon tandem solar cell with 24, 4% Power Conversion Efficiency 14 (2021) 3383.
- [89] D. Dash, R. Roshan, S. Mahata, S. Mallik, S. Mahato, S. Sarkar, A compact JV model for solar cell to simplify parameter calculation, *J. Renew. Sustain. Energy* 7 (2015) 013127.
- [90] S.K. Agnihotri, D.V. Prashant, D.P. Samajdar, Theoretical insights into the coupled optoelectronic analysis of InP truncated nanopyramid/germanium tandem solar cells, *Sol. Energy* 249 (2023) 327–335.
- [91] A. Bauer, J. Hanisch, E. Ahlswede, An effective single solar cell equivalent circuit model for two or more solar cells connected in series, *IEEE J. Photovoltaics* 4 (2013) 340–347.